

## Environmental Dependence of Galactic Properties Traced by Ly $\alpha$ Forest Absorption: Diversity among Galaxy Populations

RIEKO MOMOSE,<sup>1</sup> KAZUHIRO SHIMASAKU,<sup>1,2</sup> NOBUNARI KASHIKAWA,<sup>1,2</sup> KENTARO NAGAMINE,<sup>3,4,5</sup> IKKOH SHIMIZU,<sup>6,7</sup>  
KIMIHIKO NAKAJIMA,<sup>7,8,9</sup> YASUNORI TERAO,<sup>10</sup> HARUKA KUSAKABE,<sup>11</sup> MAKOTO ANDO,<sup>1</sup> KENTARO MOTOHARA,<sup>7,10</sup>  
LEE SPITLER,<sup>12,13</sup>

<sup>1</sup>*Department of Astronomy, School of Science, The University of Tokyo, 7-3-1 Hongo, Bunkyo-ku, Tokyo 113-0033, Japan*

<sup>2</sup>*Research Center for the Early Universe, The University of Tokyo, 7-3-1 Hongo, Bunkyo-ku, Tokyo 113-0033, Japan*

<sup>3</sup>*Theoretical Astrophysics, Department of Earth and Space Science, Osaka University, 1-1 Machikaneyama,  
Toyonaka, Osaka 560-0043, Japan*

<sup>4</sup>*Department of Physics and Astronomy, University of Nevada, Las Vegas, NV 89154-4002, USA*

<sup>5</sup>*Kavli-IPMU (WPI), The University of Tokyo, 5-1-5 Kashiwanoha, Kashiwa, Chiba 277-8583, Japan*

<sup>6</sup>*Shikoku Gakuin University, 3-2-1 Bunkyocho, Zentsuji, Kagawa 765-0013, Japan*

<sup>7</sup>*National Astronomical Observatory of Japan, 2-21-1 Osawa, Mitaka, Tokyo 181-8588, Japan*

<sup>8</sup>*Niels Bohr Institute, University of Copenhagen, Lyngbyvej 2, DK-2100 Copenhagen Ø, Denmark*

<sup>9</sup>*Cosmic DAWN Center, Denmark*

<sup>10</sup>*Institute of Astronomy, Graduate School of Science, The University of Tokyo, 2-21-1 Osawa, Mitaka, Tokyo 181-0015, Japan*

<sup>11</sup>*Observatoire de Genève, Université de Genève, 51 chemin de Pégase, 1290 Versoix, Switzerland*

<sup>12</sup>*Research Centre for Astronomy, Astrophysics & Astrophotonics, Macquarie University, Sydney, NSW 2109, Australia*

<sup>13</sup>*Department of Physics & Astronomy, Macquarie University, Sydney, NSW 2109, Australia*

### ABSTRACT

In order to shed light on how galactic properties depend on the intergalactic medium (IGM) environment traced by the Ly $\alpha$  forest, we observationally investigate the IGM–galaxy connection using the publicly available 3D IGM tomography data (CLAMATO) and several galaxy catalogs in the COSMOS field. We measure the cross-correlation function (CCF) for 570 galaxies with spec- $z$  measurements and detect a correlation with the IGM up to  $50 h^{-1}$  comoving Mpc. We show that galaxies with stellar masses of  $10^9 - 10^{10} M_{\odot}$  are the dominant contributor to the total CCF signal. We also investigate CCFs for several galaxy populations: Ly $\alpha$  emitters (LAEs), H $\alpha$  emitters (HAEs), [O III] emitters (O3Es), active galactic nuclei (AGNs), and submillimeter galaxies (SMGs), and we detect the highest signal in AGNs and SMGs at large scales ( $r \geq 5 h^{-1}$  Mpc), but in LAEs at small scales ( $r < 5 h^{-1}$  Mpc). We find that they live in various IGM environments – HAEs trace the IGM in a similar manner to the continuum-selected galaxies, but LAEs and O3Es tend to reside in higher-density regions. Additionally, LAEs’ CCF is flat up to  $r \sim 3 h^{-1}$  Mpc, indicating that they tend to avoid the highest-density regions. For AGNs and SMGs, the CCF peak at  $r = 5 - 6 h^{-1}$  Mpc implies that they tend to be in locally lower-density regions. We suspect that it is due to the photoionization of IGM HI by AGNs, i.e., the proximity effect.

*Keywords:* galaxies: formation – evolution – intergalactic medium, quasars: absorption lines, cosmology: large-scale structure of universe

### 1. INTRODUCTION

The link between the intergalactic medium (IGM) and galaxies is key to understanding the evolution of bary-

onic matter and galaxies. This is because the IGM and galaxies continuously interact with each other — galaxies are formed from condensed gas, increase their baryonic mass by accruing gas from the IGM, and pollute the surrounding IGM with metals.

Observationally, the IGM gas can be probed by Ly $\alpha$  forest absorption in background quasars’ (QSOs) and bright galaxies’ spectra, which originates from the neu-

tral atoms in photo-ionized gas (e.g., Miralda-Escudé et al. 1996; Rauch 1998). Its connection with galaxies has been investigated from the nearby universe to high redshift ( $z = 6$ ) in the literature (e.g., Adelberger et al. 2003, 2005; Chen et al. 2005; Ryan-Weber 2006; Wilman et al. 2007; Faucher-Giguère et al. 2008; Chen & Mulchaey 2009; Rakic et al. 2011, 2012; Rudie et al. 2012; Font-Ribera et al. 2013; Prochaska et al. 2013; Tejos et al. 2014; Bielby et al. 2017; Meyer et al. 2019b,a).

In particular, the IGM–galaxy connection has been examined by paying attention to overdense regions of galaxies (e.g., Stark et al. 2015; Cai et al. 2016; Lee et al. 2016). Cucciati et al. (2014) have found a significant Ly $\alpha$  absorption feature at the redshift of a protocluster in a stacked spectrum of galaxies behind the protocluster. Mawatari et al. (2017) have evaluated the IGM absorption enhancement with photometric images for the SSA22, Great Observatory Optic Deep Survey North (GOODS-N; Dickinson et al. 2004), and Subaru/XMM-Newton Deep Survey (SXDS; Furusawa et al. 2008) fields. They have found a clear enhancement of the IGM neutral hydrogen (HI) in the confirmed high galaxy density structure SSA22, but not in the remaining two fields. Those studies have shown the presence of an IGM HI overdensity in cluster regions, and vice versa (e.g., Cai et al. 2016; Hayashino et al. 2019). Using the spectra taken by the Baryon Oscillations Spectroscopic Survey project (Dawson et al. 2013) of the Sloan Digital Sky Survey III (Eisenstein et al. 2011), Cai et al. (2016) have identified IGM overdense regions from the optical depth of IGM HI, and confirmed that those regions are also overdense in galaxies. Lee et al. (2016) have found that an IGM overdensity region in their 3D tomography data of Ly $\alpha$  forest absorption coincides with a known protocluster at  $z = 2.45$  (Diener et al. 2015; Chiang et al. 2015).

The IGM–galaxy connection in the low-density environments of the field has been examined by cross-correlation between Ly $\alpha$  forest absorption and galaxies (e.g., Adelberger et al. 2005; Font-Ribera et al. 2012, 2013; Tejos et al. 2014; Bielby et al. 2017; Mukae et al. 2020). Particularly, those studies have targeted specific galaxy populations, such as QSOs (Font-Ribera et al. 2013; Prochaska et al. 2013), Lyman-break galaxies (LBGs) at  $z = 2 - 3$  (Adelberger et al. 2003, 2005; the Keck Baryonic Structure Survey, KBSS; e.g., Rakic et al. 2011, 2012; Turner et al. 2014; the VLT LBG Redshift Survey, VLRS; e.g., Crighton et al. 2011; Tumuangpak et al. 2014; Bielby et al. 2017), and damped Ly $\alpha$  systems (DLAs) at  $z < 1$  (Font-Ribera et al. 2012; Rubin et al. 2015; Pérez-Ràfols et al. 2018; Alonso et al.

2018). Those studies have detected a cross-correlation signal up to several tens of comoving  $h^{-1}$  Mpc scales.

An alternative method for investigating the IGM–galaxy connection has been introduced by Mukae et al. (2017), which enabled a comparison between the large-scale spatial distributions of galaxies and the IGM. They have compared IGM-overdensity  $\delta_{\text{F}}$  and galaxy-overdensity ( $\delta_{\text{galaxy}}$ ) evaluated from a cylinder of  $\sim 8.8$  comoving  $h^{-1}$  Mpc radius with  $\sim 88$  comoving  $h^{-1}$  Mpc depth at  $z \sim 2.5$  and found an anti-correlation between these two parameters. They have suggested that the correlation is produced by filamentary large-scale structures of both the IGM and galaxies along the sightline.

Those previous studies have successfully identified the presence of IGM–galaxy connection, which continues to tens of comoving  $h^{-1}$  Mpc scales. In addition, several studies have found some variation in the connection depending on galactic properties (e.g., Adelberger et al. 2003, 2005; Chen et al. 2005; Chen & Mulchaey 2009; Tejos et al. 2014). However, the understanding of their variation over galaxy properties and populations is limited. In order to shed more light on the IGM–galaxy connection, we examine the connection between the IGM and galaxies using observational data. We use the publicly available Ly $\alpha$  forest 3D tomography data of the COSMOS Ly $\alpha$  Mapping And Tomography Observations (CLAMATO; Lee et al. 2014, 2016, 2018) as the IGM gas and several galaxy catalogs in the literature. Because we also compare the stellar mass and star formation rate (SFR) dependence of the IGM–galaxy cross-correlation function (CCF) obtained in this paper with that predicted from cosmological hydrodynamical simulations (Momose et al. 2020), we adopt the same stellar mass and SFR binning as used in Momose et al. (2020).

Our paper consists of the following sections. We introduce the data used in this study in Section 2, and the methodology in Section 3. Observational results are shown in Section 4. Discussion and implications indicated from our results are presented in Section 5. Finally, a summary is given in Section 6. Throughout this paper, we use a cosmological parameter set of  $(\Omega_{\text{m}}, \Omega_{\Lambda}, h) = (0.31, 0.69, 0.7)$ , which has been adopted in the CLAMATO data (Lee et al. 2016, 2018). All distances are comoving, unless otherwise stated. In this paper, “cosmic web” and “IGM” indicate those traced by neutral HI gas unless otherwise specified.

## 2. DATA

### 2.1. *The IGM Data*

We use the CLAMATO data as a tracer of IGM HI gas (Lee et al. 2016, 2018)<sup>1</sup>. The CLAMATO is a 3D tomography map of  $\delta_F$  over  $2.05 < z < 2.55$  in  $0.157 \text{ deg}^2$  of the COSMOS field (Scoville et al. 2007). Here,  $\delta_F$  is the Ly $\alpha$  forest transmission fluctuation defined by

$$\delta_F = \frac{F}{\langle F_z \rangle} - 1, \quad (1)$$

where  $F$  and  $\langle F_z \rangle$  are the Ly $\alpha$  forest transmission and its cosmic mean. Lee et al. (2018) have measured  $F$  using spectra of 240 galaxies and QSOs taken with the LRIS spectrograph (Oke et al. 1995; Steidel et al. 2004) on Keck I. Those 240 background objects are at  $2.17 < z < 3.00$  and have  $[2.61, 3.18] h^{-1} \text{ Mpc}$  separations on average at  $z = 2.3$  in [R.A., decl.] directions. The effective transverse separation is  $2.04 h^{-1} \text{ Mpc}$ . The separation in the line-of-sight direction is  $2.35 h^{-1} \text{ Mpc}$  at  $z = 2.3$ . Lee et al. (2016, 2018) have evaluated  $\delta_F$  with these spatial resolutions using  $\langle F_z \rangle$  presented by Faucher-Giguère et al. (2008) and then reconstructed  $\delta_F$  with the Wiener filtering algorithm to produce a 3D tomographic map. The final 3D data cube of the CLAMATO spans comoving dimensions of  $(x, y, z) = (30, 24, 438) h^{-1} \text{ Mpc}$ , with a pixel size of  $0.5 h^{-1} \text{ Mpc}$ .

## 2.2. Galaxy Samples

We use several spec- $z$  catalogs (Lilly et al. 2007, 2009; Trump et al. 2009; Balogh et al. 2014; Le Fèvre et al. 2015; Kriek et al. 2015; Nanayakkara et al. 2016; Momcheva et al. 2016; van der Wel et al. 2016; Masters et al. 2017; Hasinger et al. 2018), two photo- $z$  catalogs (Laigle et al. 2016; Straatman et al. 2016; hereafter L16 and S16, respectively), and catalogs of Ly $\alpha$  emitters (LAEs) at  $z = 2.14 - 2.22$  (Nakajima et al. 2012, 2013; Hashimoto et al. 2013; Shibuya et al. 2014; Konno et al. 2016), H $\alpha$  emitters (HAEs) at  $z = 2.215 - 2.247$  (Sobral et al. 2013a), [OIII] $\lambda\lambda 4959, 5007$  emitters (O3Es) at  $z = 1.95 - 2.55$  (Y. Terao et al., in preparation), and submillimeter galaxies (SMGs) with spec- $z$  measurements (Smolčić et al. 2012; Brisbin et al. 2017; Michałowski et al. 2017). Galaxies with spec- $z$  measurements are used in the cross-correlation analysis (see also Section 3.1), while those with photo- $z$  estimates alone and line emitters with and without spectroscopic redshifts are used in overdensity analysis. A detailed description is given in Section 3.2. Figure 1 summarizes the catalogs used in this study, together with the catalog construction methodology. We show the redshift distributions

of our samples used in the cross-correlation analysis in Figure 2. Note that HAEs, O3Es, and active galactic nuclei (AGNs) are included in the continuum-selected galaxies in the compilation spec- $z$  catalog. The following is a detailed description of the catalogs. The number of galaxies is summarized in Tables 1 and 2.

### 2.2.1. Continuum-selected Galaxies

The cross-correlation analysis needs a spec- $z$  catalog (e.g., Momose et al. 2020). First, we compile all available spec- $z$  catalogs in the archive (Lilly et al. 2007, 2009; Trump et al. 2009; Balogh et al. 2014; Le Fèvre et al. 2015; Kriek et al. 2015; Momcheva et al. 2016; Nanayakkara et al. 2016; van der Wel et al. 2016; Masters et al. 2017; Hasinger et al. 2018) and construct one spec- $z$  catalog. We cross-match two catalogs with a maximum allowable separation of  $1''$ . If a galaxy is found in two or more catalogs, the spec- $z$  measurement obtained from near-IR observations or with a better quality flag in an original catalog is adopted. The final cross-matched spec- $z$  catalog consists of 570 galaxies. Hereafter we refer to the catalog and galaxies in it as “compiled spec- $z$  catalog” and “continuum-selected galaxies”.

For each galaxy in the compiled spec- $z$  catalog, we take stellar mass ( $M_*$ ), SFR, and specific SFR (sSFR) estimates, AGN flag, and galaxy type flag (either star-forming or quiescent) from the existing photo- $z$  catalogs of L16 and S16. Since  $M_*$  and SFR are obtained by spectral energy distribution (SED) fitting based on photometric images and depend on the set of galaxy models, we use two independent photo- $z$  catalogs of L16 and S16. Note that the survey field of L16 covers the entire CLAMATO field, while that of S16 is included in the CLAMATO field and covers only 24% of it (see also Fig. 1 in L16, Fig. 7 in S16, and Fig. 1 in Lee et al. 2018). L16 have used LEPHARE to compute photometric redshifts (Arnouts et al. 2002; Ilbert et al. 2006), while S16 have used EASY (Brammer et al. 2008). Both studies have calculated photo- $z$  and SED with near ultraviolet (NUV), optical, near-infrared (NIR), and mid-IR (MIR) data. Note that, although with a smaller survey field, S16 have used deeper NIR images and thus obtained better photo- $z$  accuracy than L16. The photo- $z$  uncertainties of L16 and S16 are  $\sigma_{\Delta z}/(1+z) = 0.021$  and  $0.009$  with catastrophic errors of 13.2 % (at  $3 < z < 6$ ) and 2.4 %, respectively. Both L16 and S16 have assumed a Chabrier (2003) initial mass function. A galaxy type either star-forming or quiescent in L16 has been determined from the color-color diagram of the NUV  $- r/r - J$  (see more detail in L16). We perform cross-matching between the compiled spec- $z$  catalog and the

<sup>1</sup> The data is from: <http://clamato.lbl.gov>

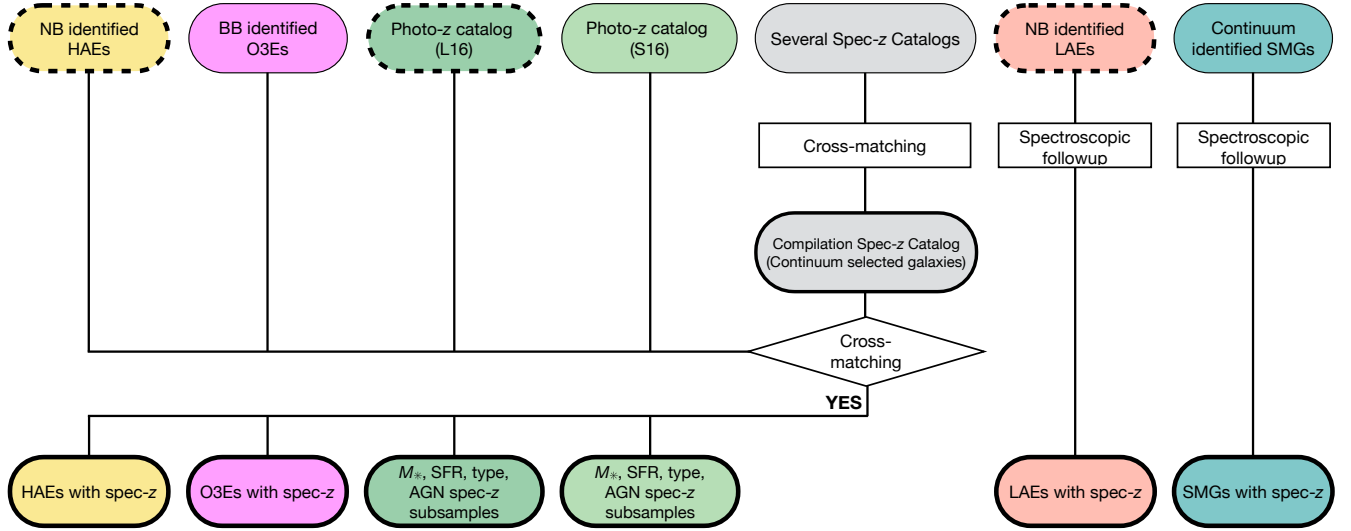


**Figure 1.** Flowchart of catalog constructions. Each color indicates a different galaxy population. Edges indicated by thick solid and thick dashed lines represent catalogs used in cross-correlation and overdensity analyses, respectively.

**Table 1.** Number of Galaxies Used in Cross-correlation Analysis

Continuum-selected	L16 <sup>a</sup>	S16 <sup>a</sup>	LAEs	HAEs	O3Es	SMGs
570	305	410	19	7	85	4

<sup>a</sup> Number of cross-matched galaxies with the compiled spec-*z* catalog.

**Table 2.** Subsamples of the L16 and S16 Spec-*z* Samples Used for Overdensity Analysis

Category	Range/Subsample	$N_{L16}$	$N_{S16}$	Sample Name
Stellar mass [ $M_{\odot}$ ]	$M_{\star} \geq 10^{11}$	11	14	$M_{\star}$ -11
	$10^{10} \leq M_{\star} < 10^{11}$	107	158	$M_{\star}$ -10
	$10^9 \leq M_{\star} < 10^{10}$	170	210	$M_{\star}$ -9
	$M_{\star} < 10^9$	9	7	$M_{\star}$ -8
$\log(\text{SFR}/M_{\odot} \text{ yr}^{-1})$	$2 \leq \log \text{SFR}$	23	5	SFR-(i)
	$1 \leq \log \text{SFR} < 2$	207	113	SFR-(ii)
	$0 \leq \log \text{SFR} < 1$	56	210	SFR-(iii)
	$0 > \log \text{SFR}$	11	60	SFR-(iv)
$\log(\text{sSFR}/\text{yr}^{-1})$	$-9 \leq \log \text{sSFR}$	245	138	sSFR-(i)
	$-10 \leq \log \text{sSFR} < -9$	39	191	sSFR-(ii)
	$-10 > \log \text{sSFR}$	11	59	sSFR-(iii)
AGNs	Total	8	21	AGN
	X-ray identified	8	16	-
	IR identified	0	8	-
Galaxy type	Star-forming	284	389	SFG
	Quiescent	13	-	QG

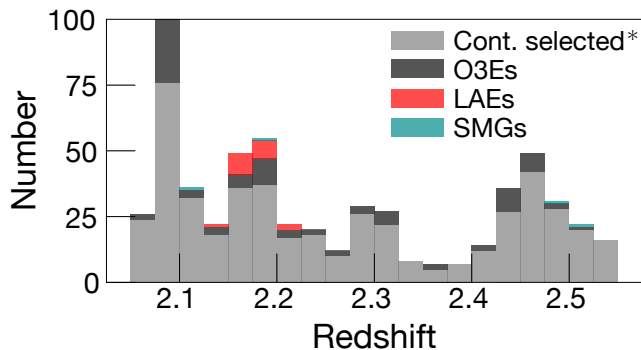


**Figure 2.** Stacked number histogram of our sample galaxies used in cross-correlation analysis as a function of redshift. Note that O3Es are included in continuum-selected galaxies. Thus, the actual number of continuum-selected galaxies is the sum of Cont. selected\* (light gray) and O3Es (dark gray).

photo- $z$  catalogs with a radius of  $0''.5$ ; 305 and 410 galaxies in the compiled spec- $z$  catalog are cross-matched with L16 and S16, respectively. We should note that owing to the deeper limiting magnitude in  $K_S$  band of S16, they have detected about a factor of 4 more objects than L16 (see Fig.13 of S16 and Fig.7 of L16). Thus, the numbers of galaxies of L16 and S16 used in this study are similar, though S16 only cover 24% of the CLAMATO field.

There are 4715 (1934) photo- $z$  galaxies in L16 (S16) within the CLAMATO field. Nevertheless, due to large photo- $z$  errors with  $\sigma_z = 0.07$  for L16 (0.023 for S16) corresponding to 61 (21)  $h^{-1}$  Mpc at  $z = 2.3$ , we only use them for overdensity analysis.

### 2.2.2. AGNs

We construct AGN catalogs by cross-matching L16 and S16 with the compiled spec- $z$  catalog. Finally, we have 8 and 21 AGNs from L16 and S16, respectively. For L16-AGNs, we regard a galaxy with X-ray flag as an AGN, meaning that L16-AGNs are X-ray-identified AGNs. For S16-AGNs, we select galaxies with AGN flags given in S16. Because S16-AGNs have been identified by IR, radio, and X-ray emission (Cowley et al. 2016), we also use this information in the CCF analysis. Among the 21 S16-AGNs, (8, 1, 21) are identified in (IR, radio, X-ray), where four are classified as both IR and X-ray AGNs. Note that four AGNs are common to L16 and S16.

### 2.2.3. Line Emitters

There are (358, 44, 575) photometrically identified (LAEs, HAEs, O3Es) in the CLAMATO field (LAEs: Nakajima et al. 2012; Konno et al. 2016, HAEs: Sobral

et al. 2013b, O3Es: Y. Terao et al., in preparation). Note that O3Es have been identified in the S16 field that is smaller than that of CLAMATO. Among them, all LAEs and HAEs are used for overdensity analysis; note that we do not use O3Es for the analysis, because they have been found by an excess of a broad-band filter, which covers a much wider redshift range with  $1.95 < z < 2.55$ . For cross-correlation analysis, we only use those with spec- $z$  measurements at  $2.05 < z < 2.55$ .

Spec- $z$  measurements of LAEs are taken from Hashimoto et al. (2013), Nakajima et al. (2013), and Shibuya et al. (2014). Among the 358 narrow-band ( $NB$ ) identified LAEs, only 19 have spec- $z$  measurements. We should note that we only use LAEs whose redshifts are determined not by  $\text{Ly}\alpha$  line but by nebular lines (e.g.,  $\text{H}\alpha$  and  $[\text{OIII}]$ ) for the cross-correlation analysis, because the redshift by  $\text{Ly}\alpha$  line is known to be larger by more than  $100 \text{ km s}^{-1}$  than the systemic redshift measured by nebular lines (e.g., Finkelstein et al. 2011; McLinden et al. 2011; Hashimoto et al. 2013, 2015; Erb et al. 2014; Shibuya et al. 2014; Song et al. 2014).

Unfortunately, no spectroscopic redshifts are given in the original HAE and O3E catalogs. Thus, we conduct cross-matching of their catalogs with the compiled spec- $z$  catalog using a searching radius of  $0''.5$ , which is the same value as used for cross-matching with the photo- $z$  catalogs. Among the 44 HAEs (575 O3Es), 7 (85) have spec- $z$  measurements. The redshifts of two HAEs among the seven are not in the range expected from the full-width half maximum (FWHM) of the  $NB$  filter, but still in the range where the filter has a sensitivity. In addition, no galaxies are found within  $2''$  radius around them. Hence, we include those two HAEs for cross-correlation analysis. We should also note that two O3Es each have two counterparts in the compiled spec- $z$  catalog. We adopt the redshift of the galaxy that is closer to the position of the O3E. The contribution by those two O3Es to our CCFs is, however, negligible.

Our emitter samples, particularly those with spec- $z$  measurements, may be dual or triple emitters. For instance, all of our LAEs with spec- $z$  measurements have  $\text{H}\alpha$  and/or  $[\text{OIII}]$  detections and thus can be also regarded as HAEs and/or O3Es. However, in this study, we classify emitters based on their first identification by photometric images owing to the lack of luminosity or equivalent width ( $EW$ ) measurements by other emission lines. For example, LAEs with spec- $z$  measurements are not included in either the HAE or O3E sample.

In order to assess whether line-emitting galaxies with spec- $z$  measurements represent their parent sample, we compare luminosity ( $L_{\text{Ly}\alpha}$ ,  $L_{\text{H}\alpha}$ , and  $L_{[\text{OIII}]\lambda 5007}$ ) and  $EW$  ( $EW_{\text{Ly}\alpha}$ ,  $EW_{\text{H}\alpha}$ , and  $EW_{[\text{OIII}]\lambda 5007}$ ) between the

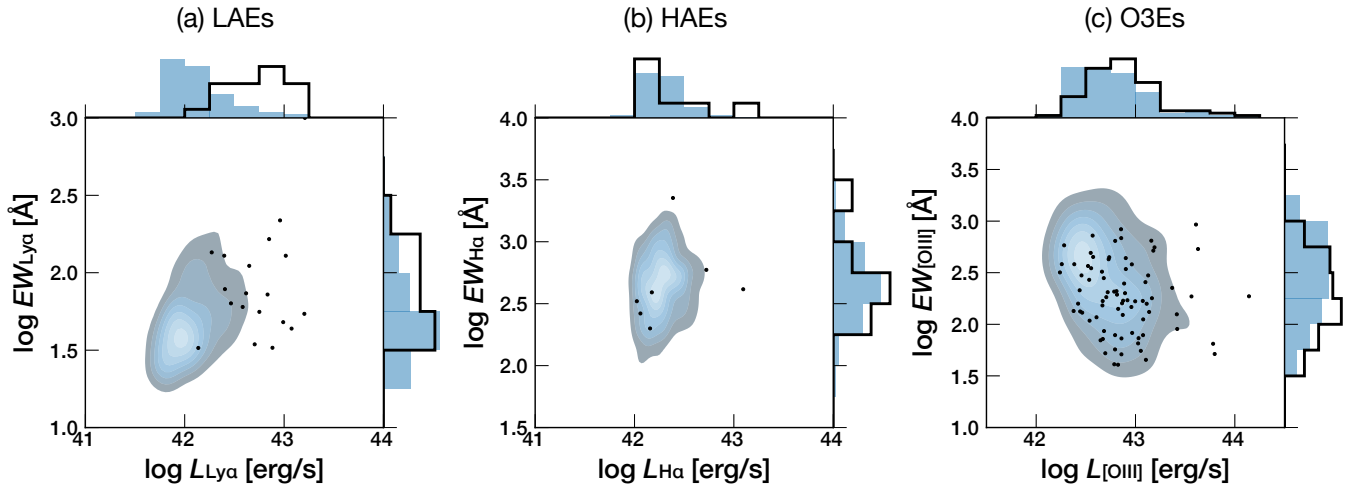


**Figure 3.** Distribution of the luminosity and  $EW$  of (a) LAEs, (b) HAEs, and (c) O3Es with and without spec- $z$  measurements. Contours are for all emitters, while black dots are for those with spec- $z$  measurements. Filled and open histograms indicate all and spec- $z$  emitters, respectively.

parent and spec- $z$  samples in Figure 3. We find LAEs with spec- $z$  measurements to be biased toward high Ly $\alpha$  luminosities. The difference in the  $L_{\text{Ly}\alpha}$  distribution is also confirmed by the Kolmogorov-Smirnov (KS) test, which gives  $p$ -values of  $9.4 \times 10^{-9}$  and 0.02 for the  $L_{\text{Ly}\alpha}$  and  $EW_{\text{Ly}\alpha}$  distributions, respectively. Similarly, O3Es with spec- $z$  measurements are biased toward higher [OIII]  $\lambda\lambda 5007$  luminosities with  $p$ -values of  $9.6 \times 10^{-3}$  and 0.03 for the  $L_{[\text{OIII}]\lambda\lambda 5007}$  and  $EW_{[\text{OIII}]\lambda\lambda 5007}$  distributions. For HAEs, on the other hand, we do not find a clear difference in either the luminosity or  $EW$  distribution.

#### 2.2.4. SMGs

We find 24 SMGs in the spec- $z$  catalogs within the CLAMATO volume (Smolčić et al. 2012; Brisbin et al. 2017; Michałowski et al. 2017). However, most of them have a relatively large spec- $z$  error ( $\sigma_z > 0.1$ ). Therefore, we only use four SMGs whose redshifts have been measured by NIR or optical spectroscopy with a sufficiently small error ( $\sigma_z \leq 0.0023$  corresponding to  $2 h^{-1}$  Mpc at  $z = 2.3$ ).

### 3. METHODOLOGY

In order to investigate the connection between the IGM and galaxies, we apply two methods – we refer to them as “cross-correlation analysis” and “overdensity analysis”. Each method is introduced in the following subsections in detail.

#### 3.1. Cross-Correlation Analysis

The first method is the cross-correlation between CLAMATO and galaxies with spec- $z$  measurements.

The CCF used in this study is

$$\xi_{\delta\text{F}}(r) = \frac{1}{\sum_{i=1}^{N(r)} \omega_{g,i}} \sum_{i=1}^{N(r)} \omega_{g,i} \delta_{g,i} - \frac{1}{\sum_{j=1}^{M(r)} \omega_{ran,j}} \sum_{j=1}^{M(r)} \omega_{ran,j} \delta_{ran,j} \quad (2)$$

$$\omega_{g,i} = \frac{1}{(\sigma_{g,i})^2}, \quad \omega_{ran,j} = \frac{1}{(\sigma_{ran,j})^2} \quad (3)$$

where  $\xi_{\delta\text{F}}$  is the cross-correlation at a separation  $r$ ;  $\delta_{g,i}$  ( $\delta_{ran,j}$ ) and  $\sigma_{g,i}$  ( $\sigma_{ran,j}$ ) are the Ly $\alpha$  forest transmission fluctuation at a place  $i$  ( $j$ ) separated by  $r$  from a galaxy (random point) and its error, respectively. Here,  $N(r)$  and  $M(r)$  represent the numbers of pixel-galaxy and pixel-random pairs with separation  $r$ , respectively. We adopt the CLAMATO’s 3D noise standard deviation measurements  $\sigma$  as  $\sigma_g(r)$  and  $\sigma_{ran}(r)$ . The CLAMATO’s standard deviation cube includes pixel noise, finite skewer sampling, and the intrinsic variance of the Ly $\alpha$  forest (see details in Lee et al. 2018). Note that  $r$  used for the cross-correlation analysis is 3D radius. This method is often adopted to measure the large-scale Ly $\alpha$  intensity (e.g., Croft et al. 2016, 2018; Kakuma et al. 2019). We calculate  $\xi_{\delta\text{F}}$  for a series of spherical shells from  $r = 1.3$  to  $100$  ( $10^{0.1}$  to  $10^2$ )  $h^{-1}$  Mpc with a  $\Delta \log(r/h^{-1} \text{ Mpc}) = 0.1$  interval.

The statistical errors in the CCF are evaluated using the jackknife resampling method. Usually, jackknife resampling for the spatial cross-correlation is performed by dividing the survey volume into several small subvolumes and removing one at a time. However, this usual method gives extremely small errors, because our

galaxy samples are small and their sky distribution is biased toward regions where intensive spec- $z$  follow-up observations have been conducted. Instead, we perform resampling by removing one object from the given sample and calculating a CCF, and by repeating this process for the number of objects in the sample. This means that the number of jackknife samples in each sample presented in Tables 1 and 2 is the same as that of galaxies in it. Because of that, the CCF errors in this study are dominated by the small sample sizes.

### 3.2. Overdensity Analysis

Because our samples of galaxies with spec- $z$  measurements are very limited, we also apply another analysis to use as many galaxies as possible. This second method compares mean IGM fluctuations ( $\langle\delta_F\rangle$ ) and galaxy overdensities within randomly distributed cylinders (Mukae et al. 2017), and can be applied to photometric redshift samples whose redshift uncertainties  $\sigma_z$  are less than 0.1. In this study, we focus only on two redshift ranges of  $2.14 < z < 2.22$  and  $2.215 < z < 2.247$ , which are defined by the central wavelength and FWHM of the  $NB$  filters for LAEs and HAEs. Additionally, we only use photo- $z$  galaxies of L16 for the overdensity analysis, because the survey area of S16 is smaller than CLAMATO’s coverage. The number of galaxies used in the analysis is shown in Tables 3 or 4.

We first collapse each of the CLAMATO data of the above two redshift ranges in the redshift direction to generate a 2D map, where the thickness of the original data,  $\Delta z = 0.08$  (0.032), corresponds to  $69.7$  ( $27.9$ )  $h^{-1}$  Mpc for LAEs (HAEs). Then, for each 2D map, we identify local minima and maxima of the IGM fluctuations and calculate  $\langle\delta_F\rangle$  within a circle of radius  $r$  centered at them. Since the original data have a thickness of  $\Delta z$ ,  $\langle\delta_F\rangle$  effectively means the mean IGM fluctuations within a cylinder whose volume is  $\Delta z \times \pi r^2$  and is calculated with

$$\langle\delta_F\rangle = \frac{1}{\sum_{i=1}^{N(r)} \omega_{g,i}(r)} \sum_{i=1}^{N(r)} \omega_{g,i}(r) \delta_{g,i}(r), \quad (4)$$

where  $\delta_{g,i}$  and  $\omega_{g,i}$  are the same as in Equations 2 and 3 but obtained from the 2D CLAMATO map. We should note that we also generate 2D standard deviation maps in order to evaluate  $\omega_{g,i}$  from the 2D map. For a direct comparison between the above two redshift ranges, we calculate  $\langle\delta_F\rangle$  with the same volume by adopting a different cylinder radius, that is, 3 and  $4.74 h^{-1}$  Mpc for  $2.14 < z < 2.22$  and  $2.215 < z < 2.247$ , respectively. The radii are determined to satisfy three requirements: i) they are larger than the transverse resolution of the

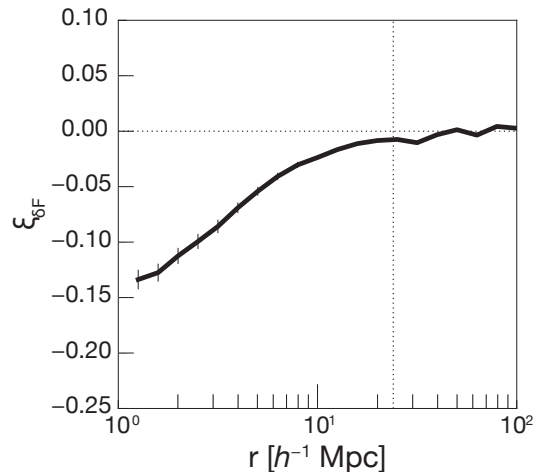


**Figure 4.** The CCF of all galaxies in our compiled spec- $z$  catalog. A vertical dotted line shows the possible largest radius for 3D cross-correlation calculations. Beyond this radius, the majority of  $\delta_F$  values are from the line-of-sight direction.

CLAMATO data (see Section 2.1), ii) they are sufficiently small so that neighboring cylinders do not significantly overlap with each other, and iii) requirements i) and ii) are satisfied in both two redshift ranges.

Galaxy overdensities are evaluated within the same cylinders. We calculate galaxy overdensity ( $\Sigma_{\text{gal}}$ ) with

$$\Sigma_{\text{gal}} = \frac{N_{\text{gal}}}{\langle N_{\text{gal}} \rangle} - 1, \quad (5)$$

where  $N_{\text{gal}}$  is the number of galaxies in the cylinder and  $\langle N_{\text{gal}} \rangle$  is the mean number of galaxies expected to be found in the same volume. We estimate the error of  $\Sigma_{\text{gal}}$  with the Poisson errors. Note that we do not consider any photo- $z$  uncertainties including catastrophic errors here, because they influence both  $N_{\text{gal}}$  and  $\langle N_{\text{gal}} \rangle$  estimates. Qualitatively, those errors will weaken the contrast of galaxy over/underdensities, which results in a narrower dynamic range of  $\Sigma_{\text{gal}}$ .

In order to examine whether the measured correlation is biased owing to using only local maxima and minima positions, we also investigate the  $\langle\delta_F\rangle$ - $\Sigma_{\text{gal}}$  relation based on randomly chosen cylinder positions (see also Mukae et al. 2017). If photo- $z$  measurements are valid with smaller errors than the cylinder depth, the bias should be negligible (Mukae et al. 2017; Momose et al. 2020).

## 4. RESULTS

### 4.1. Cross-correlation Analysis

In this section, we show results of the cross-correlation analysis. Figure 4 shows the CCF from all galaxies in

**Table 3.** Measurement results of overdensity analysis from local minima and maxima.

Sample	$N_1^{(1)}$	$N_2^{(2)}$	$R_s^{(3)}$	$p^{(3)}$	$\alpha^{(4)}$	$\beta^{(4)}$
L16- $M_*$ -10	137	41	-0.31	0.30	$0.003 \pm 0.011$	$-0.061 \pm 0.023$
L16- $M_*$ -9	462	159	-0.54	0.05	$-0.006 \pm 0.010$	$-0.121 \pm 0.040$
L16- $M_*$ -8	266	86	-0.17	0.58	$-0.009 \pm 0.012$	$-0.016 \pm 0.034$
ALL	865	286	-0.47	0.10	$-0.006 \pm 0.011$	$-0.085 \pm 0.040$
LAEs	358	-	-0.70	0.19	$-0.088 \pm 0.021$	$-0.147 \pm 0.054$
HAEs	-	44	-0.19	0.65	$-0.002 \pm 0.014$	$-0.010 \pm 0.023$

<sup>(1)</sup> Number of galaxies in  $2.14 < z < 2.22$ . <sup>(2)</sup> Number of galaxies in  $2.215 < z < 2.247$ . <sup>(3)</sup> Spearman’s coefficient and  $p$ -value for the  $\langle \delta_F \rangle - \delta_{\text{galaxy}}$  relation from local minima and maxima. <sup>(4)</sup> The best-fit parameters of chi-square fitting of the  $\langle \delta_F \rangle - \delta_{\text{galaxy}}$  relation from local minima and maxima.

**Table 4.** Measurement results of overdensity analysis from random positions.

Sample	$N_1^{(1)}$	$N_2^{(2)}$	$R_s^{(3)}$	$p^{(3)}$	$\alpha^{(4)}$	$\beta^{(4)}$
L16- $M_*$ -10	137	41	-0.79	3.75e-3	$-0.006 \pm 0.007$	$-0.057 \pm 0.011$
L16- $M_*$ -9	462	159	-0.65	0.02	$-0.014 \pm 0.007$	$-0.156 \pm 0.025$
L16- $M_*$ -8	266	86	0.21	0.49	$-0.004 \pm 0.026$	$0.424 \pm 0.237$
ALL	865	286	-0.65	0.02	$-0.011 \pm 0.007$	$-0.170 \pm 0.029$
LAEs	358	-	-0.70	0.19	$-0.054 \pm 0.011$	$-0.059 \pm 0.043$
HAEs	-	44	-0.26	0.53	$-0.003 \pm 0.018$	$-0.038 \pm 0.037$

<sup>(1)</sup> Number of galaxies in  $2.14 < z < 2.22$ . <sup>(2)</sup> Number of galaxies in  $2.215 < z < 2.247$ . <sup>(3)</sup> Spearman’s coefficient and  $p$ -value for the  $\langle \delta_F \rangle - \delta_{\text{galaxy}}$  relation from random points. <sup>(4)</sup> The best-fit parameters of chi-square fitting of the  $\langle \delta_F \rangle - \delta_{\text{galaxy}}$  relation from random points.

the compiled spec- $z$  catalog. A strong signal is detected at the center with  $\xi_{\delta_F} = -0.14$ . The CCF increases monotonically and reaches the cosmic mean ( $\xi_{\delta_F} = 0$ ) at  $r \sim 50 \text{ Mpc } h^{-1}$ . If the IGM HI density around galaxies is higher than the mean HI density, the CCF has a negative value because of stronger Ly $\alpha$  absorption. Thus, Figure 4 indicates that galaxies are in HI overdensity regions on average up to  $\sim 50 h^{-1} \text{ Mpc}$  in radius. We should note that we cannot calculate a CCF three-dimensionally over  $r > 12 h^{-1} \text{ Mpc}$  because of the limitation of the CLAMATO volume.

#### 4.1.1. Galaxy Properties

For more detailed investigations depending on galaxy properties, we divide the L16 and S16 samples into four or three subsamples based on  $M_*$ , SFR, sSFR, and galaxy type (star-forming or quiescent galaxy, hereafter SFG or QG). For a direct comparison with the results from hydrodynamical simulations given in Momose et al. (2020), we set the subsample ranges to be basically the same as those used in Momose et al. (2020). The number of galaxies in each subsample and its sample name are listed in Table 2. We show the CCFs of individual samples in Figure 5. Because we take  $M_*$ , SFR, and

sSFR values from both L16 and S16, we regard a sample for which L16 and S16 give consistent CCFs as being reliable.

For all the subsamples, we detect a signal up to  $r = 10 - 20 h^{-1} \text{ Mpc}$ . Nevertheless, we do not find any trends depending on  $M_*$ , SFR, or sSFR for either L16 or S16. In addition, due to the large error bars in several subsamples ( $M_*$ -11,  $M_*$ -8, SFR-(i), SFR-(iv), L16-sSFR-(iii), and L16-QG), the variation of the CCF depending on mass, SFR, and sSFR that has been confirmed in the simulations (Momose et al. 2020) is insignificant. Detailed discussion on the lack of significant dependence on galactic properties is given in Section 5.2.2. Note that photo- $z$  errors do not affect the CCF calculation itself, because the calculation only uses spec- $z$  measurements as the line-of-sight positions of galaxies. However, the photo- $z$  errors affect the grouping depending on galactic properties as a contamination to subsamples. This effect seems to be larger for fainter galaxies (e.g., Fig. 21 in S16), and attenuates the dependence of the CCFs on galactic properties even if it exists (Momose et al. 2020).

For a comparison between L16 and S16, several subsamples show consistency. Among the  $M_*$  subsamples,



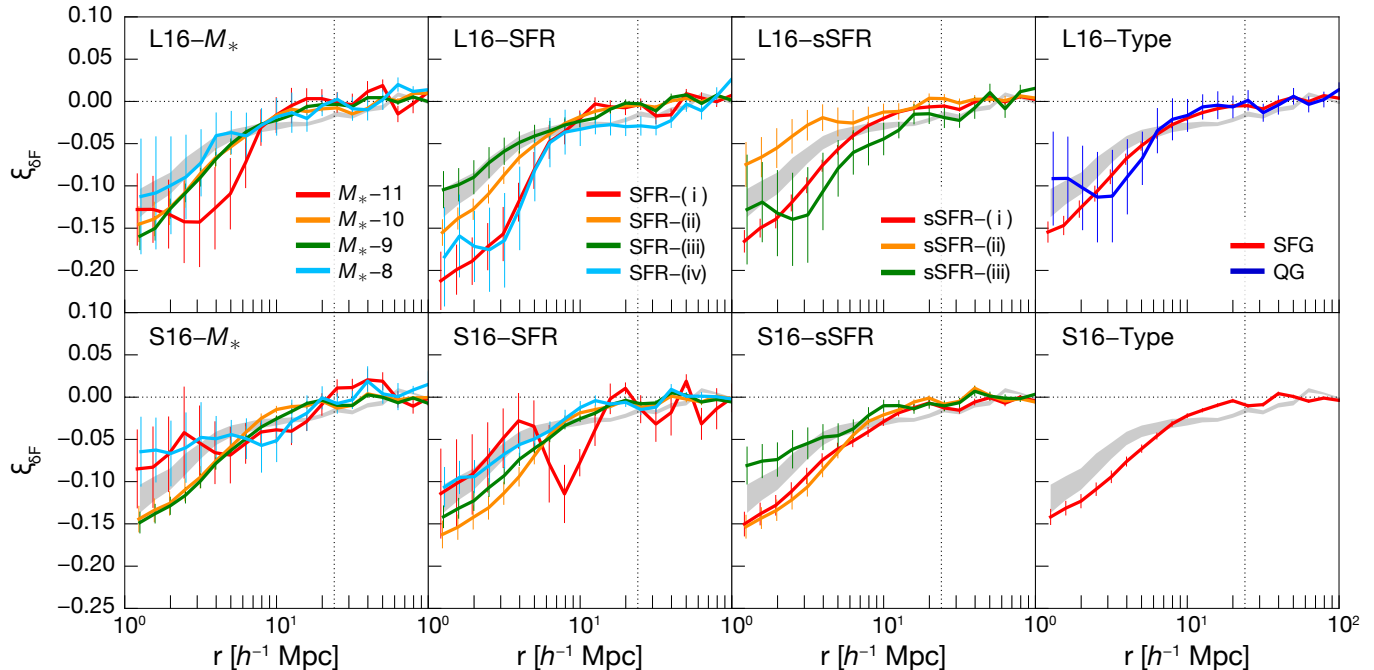


**Figure 5.** CCFs of (top) L16 and (bottom) S16 subsamples divided by  $M_*$ , SFR, sSFR, and galaxy type (from left to right) as a function of radius in comoving units. The meaning of vertical dotted lines is the same as in Figure 4. Gray shades represent the CCF of continuum-selected galaxies in the compiled spec- $z$  catalog.

the  $M_*$ -10 and  $M_*$ -9 subsamples give consistent CCFs with the strongest signal at the center,  $\xi_{\delta F} = -0.15$ , and reaching the cosmic mean at  $r = 20 - 30 h^{-1}$  Mpc. For the SFR subsamples, only the SFR-(ii) subsamples give consistent results, showing a monotonic increase with the strongest signal at the center of  $\xi_{\delta F} = -0.16$ . For the sSFR subsamples, only the sSFR-(i) subsamples give consistent results, with the strongest signal of  $\xi_{\delta F} = -0.15 - -0.17$ . The SFG subsamples of L16 and S16 show similar monotonically increasing CCFs starting from  $\xi_{\delta F} = -0.15$ .

In order to quantify the similarity or difference in the CCF between L16 and S16 subsamples and all continuum-selected galaxies, we also show the CCF of all galaxies of the compiled spec- $z$  catalog as a gray shade in Figure 5. We find that the CCFs of the  $M_*$ -10,  $M_*$ -9, SFR-(ii), SFR-(iii), sSFR-(i), S16-sSFR-(ii), and SFG subsamples are similar to that of the all galaxies of the compiled spec- $z$  catalog. This is because that star-forming galaxies with  $M_* \sim 10^{10} M_\odot$  and  $\text{SFR} \sim 10 - 100 M_\odot \text{ yr}^{-1}$  are dominant in our compiled spec- $z$  catalog (see also Table 2) and thus are responsible for the CCF in Figure 4. The other subsamples ( $M_*$ -11,  $M_*$ -8, SFR-(i), SFR-(iv), sSFR-(iii)) show a large difference between L16 and S16. We will discuss its reason in Sections 5.2.1 and 5.2.2.

#### 4.1.2. Comparison of the CCF of Continuum-selected Galaxies with Those in Cosmological Hydrodynamical Simulations

Because we do not find any significant  $M_*$ , SFR, and/or sSFR dependence in the CCFs, we compare the CCF of the continuum-selected galaxies to those obtained from cosmological hydrodynamical simulations (Momose et al. 2020).

In Figure 6, we overlay the CCF of continuum-selected galaxies (black solid line) on those of  $M_*$ , SFR, and sSFR subsamples in Momose et al. (2020) (colored lines). The definition of each subsample and its name are the same as given in Table 2 (for more details, see Table 1 of Momose et al. 2020). We also show the CCF ratios,  $\Xi = \xi_{\text{sim}}/\xi_{\text{all}}$ , at the bottom of Figure 6.

We find that the CCF of continuum-selected galaxies agrees with that of all simulated galaxies in Momose et al. (2020) over  $r = 4 - 20 h^{-1}$  Mpc. A detailed comparison with the  $M_*$ -, SFR-, and sSFR-dependent CCFs shows that the  $M_*$ -9, SFR-(iii), SFR-(iv), and sSFR-(ii) subsamples match well with the continuum-selected sample, particularly over  $r = 3 - 20 h^{-1}$  Mpc. We briefly discuss this result in Section 5.2.1.

#### 4.1.3. Galaxy Populations

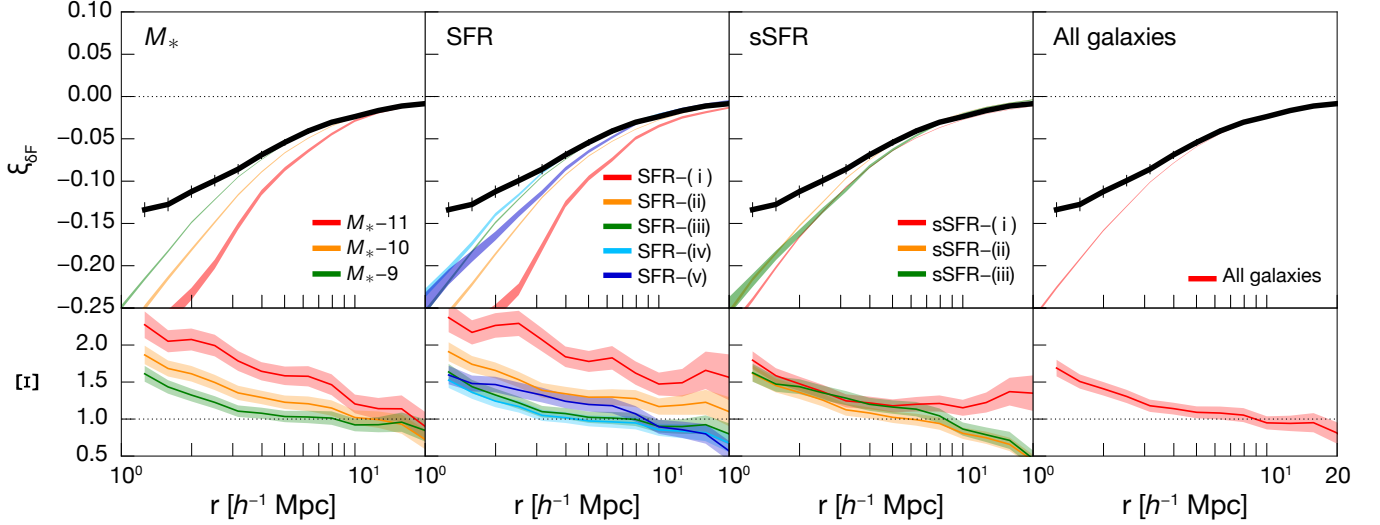


**Figure 6.** (Top) CCFs as a function of radius in comoving units from cosmological hydrodynamical simulations in Momose et al. (2020) together with that of continuum-selected galaxies in Figure 4 which is colored in black. (Bottom)  $\Xi = \xi_{\text{sim}}/\xi_{\text{all}}$ .

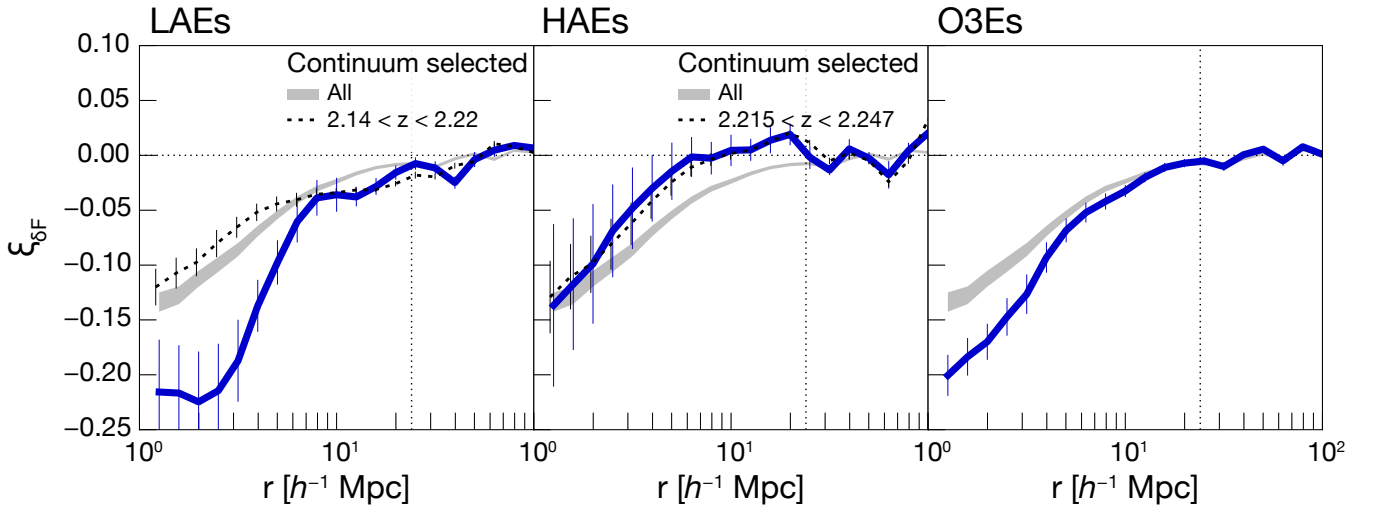


**Figure 7.** CCFs of LAEs, HAEs, and O3Es from left to right as a function of radius in comoving units. Colored in gray is the CCF of the continuum-selected galaxies. Dashed lines in LAEs and HAEs indicate CCFs obtained from galaxies at the narrow redshift ranges defined by the FWHM of  $NB$  filters. The meaning of vertical dotted lines is the same as in Figure 4.

*All Line Emitters*—Figure 7 presents the CCFs of three different emitters of LAEs, HAEs, and O3Es from the left. We also plot the CCFs of the continuum-selected galaxies by a gray shade and the CCFs of continuum-selected galaxies within the redshift range defined by the FWHM of the  $NB$  filter for LAEs at  $2.14 < z < 2.22$  (HAEs at  $2.215 < z < 2.247$ ) with a black dotted line. We refer to these redshift-specified CCFs of continuum-selected galaxies to compare the CCFs of LAEs and HAEs. Note that the CCFs of all continuum-selected galaxies from the entire CLAMATO redshift range and

the above two specific redshift ranges have different slopes, although the  $\xi_{\delta F}$  values at the center agree within the errors. We suspect that the differences in slope are due to cosmic variance (Momose et al. 2020).

We detect signals for all the emitters. However, the strength and shape of the CCFs differ from each other. LAEs show the strongest signal among the three emitter populations with  $\xi_{\delta F} = -0.23$ , which is even stronger than the CCF of the continuum-selected galaxies at the same redshift range defined by the  $NB$  filter (Nakajima et al. 2012; Konno et al. 2016). Additionally, LAEs’

CCF is clearly different from those of any other galaxies, being flat up to  $r \sim 3 h^{-1}$  Mpc followed by a monotonic increase toward the cosmic mean. The CCF of O3Es in Figure 7 (right) also shows the strongest signal with  $\xi_{\delta\text{F}} = -0.21$  which is comparable to that of LAEs within the errors. The CCF monotonically increases up to the cosmic mean at  $r \sim 20 h^{-1}$  Mpc just like that of continuum-selected galaxies. On the other hand, the CCF of HAEs agrees well with that of continuum-selected galaxies at the same redshift range defined by the *NB* filter (Sobral et al. 2013a) in both the shape and the amplitude with  $\xi_{\delta\text{F}} = -0.15$ . This agreement indicates that HAEs are distributed in the cosmic web in the same manner as continuum-selected galaxies. We will discuss it in Sections 5.2.4 and 5.3.

*LAEs*—As we note in Section 2.2, our LAEs are likely biased toward higher  $L_{\text{Ly}\alpha}$ , and thus their CCF in Figure 7 (left) could more reflect the gas environments of such luminous LAEs. To evaluate the effect of this bias, we make two subsamples according to  $\text{Ly}\alpha$  luminosity ( $L_{\text{Ly}\alpha}$ ), an  $\text{Ly}\alpha$ -luminous one with  $L_{\text{Ly}\alpha} \geq 10^{43}$  erg  $\text{s}^{-1}$  (four objects) and an  $\text{Ly}\alpha$ -faint one with  $L_{\text{Ly}\alpha} < 3 \times 10^{42}$  erg  $\text{s}^{-1}$  (five objects), and calculate the CCF for each. As found from Figure 8 (a), both the  $\text{Ly}\alpha$ -luminous and  $\text{Ly}\alpha$ -faint subsamples have stronger signals than the continuum-selected galaxies. Although consistent within the errors, the  $\text{Ly}\alpha$ -faint subsample has a slightly stronger signal than the  $\text{Ly}\alpha$ -luminous one, with a flatter CCF up to  $r \sim 3 h^{-1}$  Mpc. These results perhaps indicate that LAEs with different  $L_{\text{Ly}\alpha}$  are distributed in the cosmic web in a different manner.

To understand the IGM environments of LAEs in more detail, we conduct an additional investigation by making another four subsamples based on equivalent width ( $EW_{\text{Ly}\alpha}$ ) and UV luminosity ( $f_{\text{UV}}$ ): large- $EW_{\text{Ly}\alpha}$  ( $EW_{\text{Ly}\alpha} \geq 100$  Å, seven objects), small- $EW_{\text{Ly}\alpha}$  ( $EW_{\text{Ly}\alpha} < 40$  Å, three objects), UV-luminous ( $f_{\text{UV}} \geq 1 \times 10^{-29}$  erg  $\text{cm}^{-2}$   $\text{s}^{-1}$   $\text{Hz}^{-1}$ , four objects), and UV-faint ( $f_{\text{UV}} < 2 \times 10^{-30}$  erg  $\text{cm}^{-2}$   $\text{s}^{-1}$   $\text{Hz}^{-1}$ , four objects). The CCFs of these four subsamples are shown in Figure 8 (b) and (c). For the  $EW$  subsamples, we find a clear difference in their CCFs. The CCF of the small- $EW_{\text{Ly}\alpha}$  subsample has a similar shape to that of all LAEs, but with a stronger signal of  $\xi_{\delta\text{F}} = -0.37$ , while the CCF of the large- $EW_{\text{Ly}\alpha}$  subsample shows a good agreement with that of continuum-selected galaxies. For the UV subsamples, the UV-luminous one has a stronger signal than the UV-faint one and shows a flat CCF up to as large as  $r \sim 5 h^{-1}$  Mpc. On the other hand, the UV-faint subsample has a similar CCF shape and strength to the continuum-selected galaxies.

*O3Es*—Similar to the LAEs, our O3Es are also biased toward higher  $L_{[\text{OIII}]\lambda\lambda 5007}$ . We measure CCFs by dividing our O3Es into three subsamples based on  $L_{[\text{OIII}]\lambda\lambda 5007}$  and  $EW_{[\text{OIII}]\lambda\lambda 5007}$  in Figure 9 (a) and (b). We do not find any clear dependence on either  $L_{[\text{OIII}]\lambda\lambda 5007}$  or  $EW_{[\text{OIII}]\lambda\lambda 5007}$ .

We also compare the CCF of O3Es with those of LAEs, HAEs, and continuum-selected galaxies at  $2.14 < z < 2.22$  and  $2.215 < z < 2.247$ . The difference from Figure 7 (right) is that only O3Es in those redshift ranges are used. As shown in Figure 9 (c) and (d), the O3Es have a stronger CCF than the HAEs and a slightly weaker CCF than the LAEs.

*AGNs and SMGs*—The CCFs of AGNs and SMGs are shown in Figure 10, which are greatly different from those of continuum-selected galaxies and emitters. A common feature of the CCFs of the L16-AGNs and the S16-AGNs is a negative peak (i.e., the largest signal) at  $r \sim 5 h^{-1}$  Mpc. Although this feature of the L16-AGNs is weak, being only  $< 2\sigma$  away from the cosmic mean ( $\xi_{\delta\text{F}} = 0$ ), that of the S16-AGNs is significant with  $\xi_{\delta\text{F}} = -0.1$ . The CCF of SMGs also shows a negative peak at  $r \sim 5 - 6 h^{-1}$  Mpc with  $\xi_{\delta\text{F}} = -0.09$ . Because two of the four SMGs have an X-ray source within a  $1''$  aperture, and one of the remaining two has an X-ray source within a  $2''$  aperture, most of our SMG sample are AGNs. Thus, the strongest CCF signal at  $r \sim 5 - 6 h^{-1}$  Mpc away from the center seen in both AGNs and SMGs is probably due to the AGN activity of the central black hole and thus may be a general feature of the IGM HI around AGNs. Mukae et al. (2020) have also found  $5 - 10 h^{-1}$  Mpc off-center negative peaks around QSOs (Mukae et al. 2020). Further discussion is given in Section 5.2.6.

Figure 10 also shows an interesting trend depending on the AGN type. X-ray-identified AGNs, which are all L16-AGNs and a fraction of the S16-AGNs (dashed line), show a negative value at the center and a decrease up to  $r \sim 4 - 5 h^{-1}$  Mpc until reaching the negative peak. On the other hand, S16's IR-identified AGN and SMGs have a positive  $\xi_{\delta\text{F}}$  value at the center. It implies that X-ray-identified AGNs have a slightly stronger CCF than IR-identified one. We also discuss it in Section 5.2.6.

#### 4.1.4. Comparison of the CCFs

We show the CCFs of all galaxy populations and all continuum-selected galaxies simultaneously in Figure 11 (a) together with  $\text{Ly}\alpha$  forest-LBGs CCFs evaluated at  $z \sim 3$  in the literature (Adelberger et al. 2005; Bielby et al. 2017). For visibility purposes, we only plot the CCF of the S16-AGNs as the representative of AGNs.

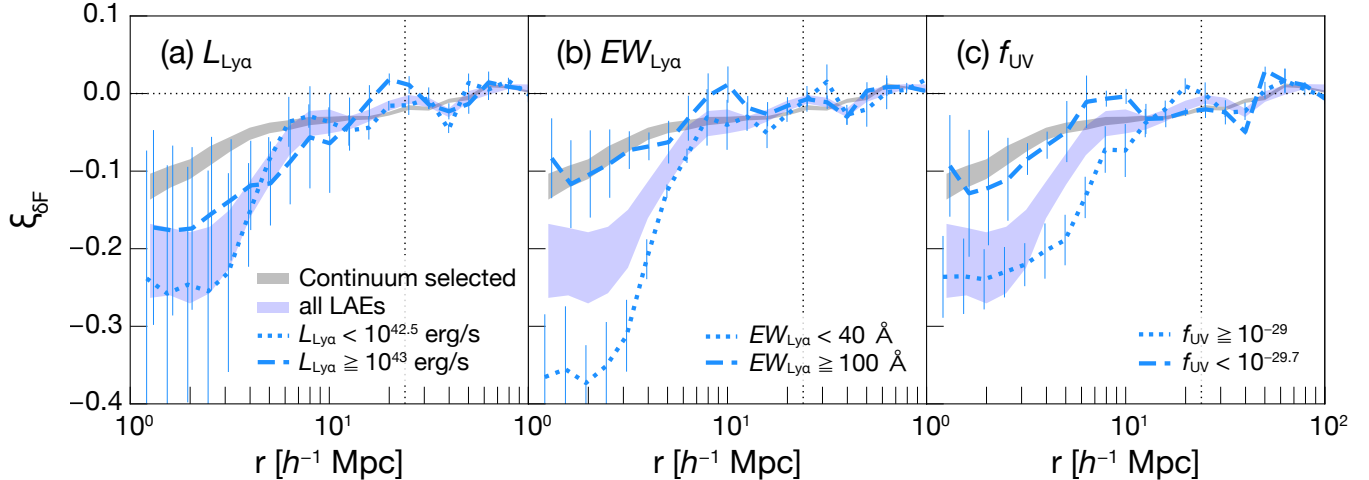


**Figure 8.** CCFs of LAE subsamples divided by (a)  $L_{\text{Ly}\alpha}$ , (b)  $EW_{\text{Ly}\alpha}$ , and (c) UV luminosity as a function of radius in comoving units. The meaning of vertical dotted lines is the same as in Figure 4.

The CCF of continuum-selected galaxies agrees well with that of LBGs at  $r > 3 h^{-1}$  Mpc, though the latter is largely scattered within  $r < 3 h^{-1}$  Mpc. However, the CCFs of other galaxy populations show a variation. In addition, all galaxy populations except HAEs have a stronger signal than the continuum-selected galaxies at  $r > 5 h^{-1}$  Mpc in Figure 11 (b).

To quantify the CCFs, we fit them by a power-law with:

$$\xi_{\delta\text{F}}(r) = \left(\frac{r}{r_0}\right)^\gamma, \quad (6)$$

where  $r_0$  and  $\gamma$  are the clustering length and slope, respectively. We fit the CCFs of star-forming galaxies (i.e., continuum-selected galaxies, LAEs, HAEs, O3Es) over  $r = 3 - 24 h^{-1}$  Mpc;  $3 h^{-1}$  Mpc corresponds to the spectral resolution of the CLAMATO and  $24 h^{-1}$  Mpc corresponds to the CLAMATO's short side on the sky. For AGNs and SMGs, we fit their CCFs over  $r = 5 - 24 h^{-1}$  Mpc, because the observed CCFs deviate from a single power-law over  $3 < r < 5 h^{-1}$  Mpc. The best-fit parameters are summarized in Table 5.

We find the best-fit parameters of continuum-selected galaxies to be  $r_0 = 0.45 \pm 0.04$  and  $\gamma = 1.23 \pm 0.04$ , which are comparable to those evaluated in the literature. Bielby et al. (2017) have calculated a CCF between Ly $\alpha$  absorption and LBGs at  $z \sim 3$  and obtained its best-fit parameters to be  $r_0 = 0.27 \pm 0.14$  and  $\gamma = 1.1 \pm 0.2$ . Tejos et al. (2014) have examined the variety of the CCFs for galaxies at  $z < 1$  depending on the HI column density of the IGM and found the best-fit parameters of weak HI systems ( $N_{\text{HI}} < 10^{14} \text{ cm}^{-2}$ ) to be  $r_0 = 0.2 \pm 0.4$  and  $\gamma = 1.1 \pm 0.3$ . However, Momose et al. (2020) have obtained slightly larger values of  $r_0 = 0.62 \pm 0.04$  and  $\gamma = 1.37 \pm 0.04$  over the same

fitting range<sup>2</sup>. We suspect that the slightly smaller best-fit parameters in this study may be due to the smearing of the CCF because of the lower effective spectral resolution of the CLAMATO than that of the simulations (Momose et al. 2020), whose line-of-sight resolution is  $0.4 h^{-1}$  Mpc at  $\langle z \rangle = 2.3$ .

All galaxy populations except HAEs are found to have a similar slope to that of continuum-selected galaxies with  $\gamma = 1.2 - 1.3$ . Nonetheless, their clustering lengths  $r_0$  are larger than those of continuum-selected galaxies. On the other hand, the best-fit parameters of HAEs agree within the errors with those of continuum-selected galaxies in the same redshift range.

#### 4.2. Overdensity Analysis

Overdensity analysis is conducted on photo- $z$  galaxies in L16 (ALL) and  $NB$ -selected LAEs and HAEs. We divide the photo- $z$  galaxies into three subsamples based on stellar mass ( $M_\star \geq 10^{10} M_\odot$ : L16- $M_\star$ -10,  $10^9 \leq M_\star/M_\odot < 10^{10}$ : L16- $M_\star$ -9,  $10^8 \leq M_\star/M_\odot < 10^9$ : L16- $M_\star$ -8). The number of galaxies in individual subsamples is shown in Tables 3 or 4. Figure 12 presents  $\langle \delta_{\text{F}} \rangle - \Sigma_{\text{gal}}$  relations for the six subsamples. We assume Poisson noise to evaluate the error in  $\Sigma_{\text{gal}}$  measurements.

We first find a negative  $\langle \delta_{\text{F}} \rangle - \Sigma_{\text{gal}}$  correlation for all six subsamples by eyes. To assess the significance of the correlation, we calculate the Spearman's rank correlation coefficient  $R_s$  for each subsample, as summarized in Table 3. We find negative  $R_s$  values for all

<sup>2</sup> Momose et al. (2020) have evaluated the best-fit parameters ( $r_0$ ,  $\gamma$ ) of the IGM regime over  $r = 0 - 10 h^{-1}$  Mpc and obtained ( $0.34 \pm 0.03$ ,  $1.07 \pm 0.04$ ). However, we recalculate them over  $r = 3 - 24 h^{-1}$  for a fair comparison with those of this study.

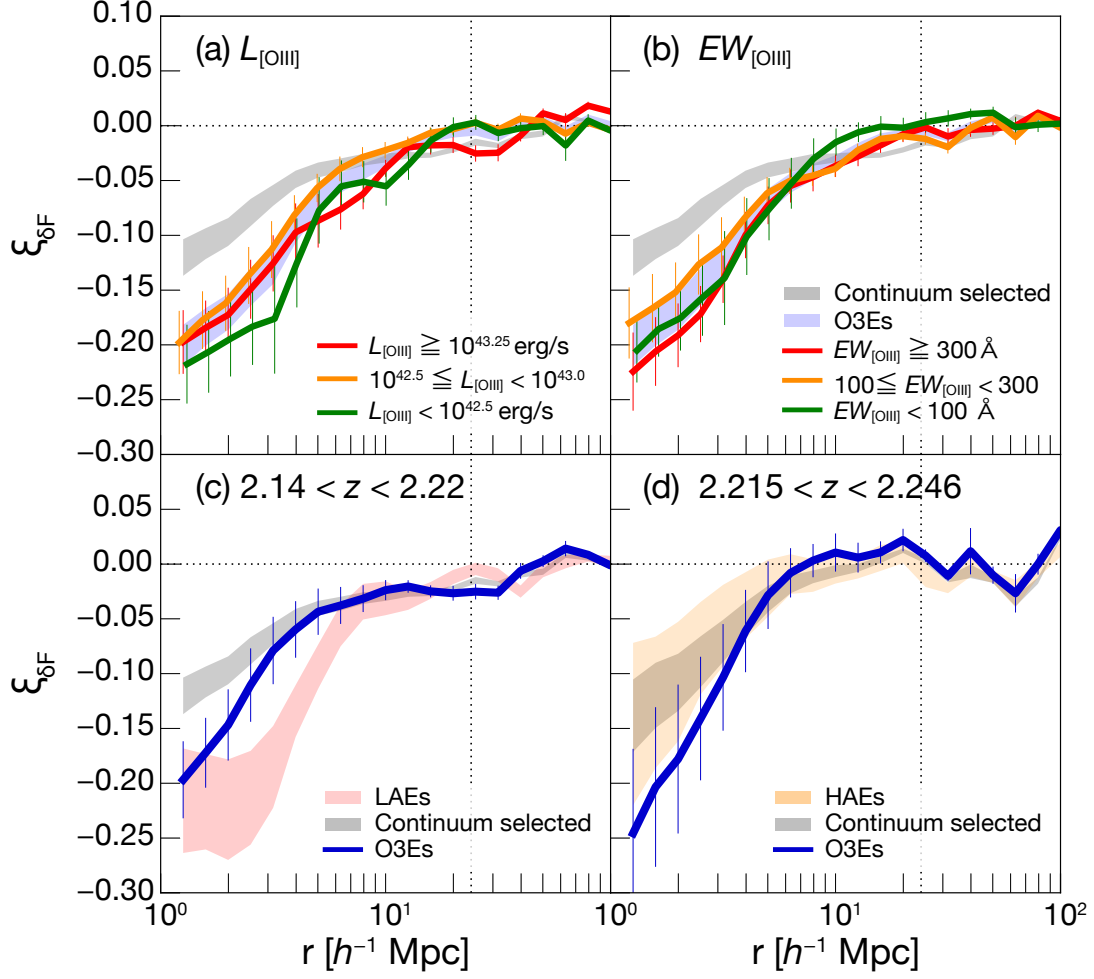


**Figure 9.** CCFs between O3Es and  $\text{Ly}\alpha$  absorption as a function of radius in comoving units. *Panel (a):*  $L_{[\text{OIII}]}$  subsamples. Gray and royal blue shades represent the CCFs of continuum-selected galaxies in the compiled spec- $z$  catalog and all O3Es, respectively. *Panel (b):*  $EW_{[\text{OIII}]}$  subsamples. Meanings of gray and royal blue shades are the same as in Panel (a). *Panel (c):* The O3E subsample is limited to the same redshift range as of LAEs,  $2.14 < z < 2.22$ . The CCF of LAEs is colored in pink. A gray shade represents the CCF of continuum-selected galaxies at  $2.14 < z < 2.22$ . *Panel (d):* For the O3E subsample in the same redshift range as of HAEs,  $2.215 < z < 2.246$ . The CCF of HAEs is colored in orange. A gray shade represents the CCF of continuum-selected galaxies at  $2.215 < z < 2.246$ . The meaning of vertical dotted lines is the same as in Figure 4.

**Table 5.** The best fit parameters of our CCFs.

Sample	$r_0$ [ $h^{-1}$ Mpc]	$\gamma$	Fitting Range [ $h^{-1}$ Mpc]
Continuum-selected galaxies	$0.46 \pm 0.04$	$1.23 \pm 0.04$	3 – 24
LAEs	$0.78 \pm 0.13$	$1.25 \pm 0.10$	3 – 24
Galaxies at $2.14 < z < 2.22$	$(2.92 \pm 2.40) \times 10^{-3}$	$0.41 \pm 0.04$	3 – 24
HAEs	$1.24 \pm 0.23$	$3.16 \pm 0.55$	3 – 24
Galaxies at $2.215 < z < 2.247$	$1.11 \pm 0.17$	$2.57 \pm 0.31$	3 – 24
O3Es	$0.72 \pm 0.09$	$1.37 \pm 0.08$	3 – 24
S16-AGN	$0.99 \pm 0.42$	$1.32 \pm 0.26$	5 – 24
SMGs	$0.41 \pm 0.26$	$0.94 \pm 0.19$	5 – 24

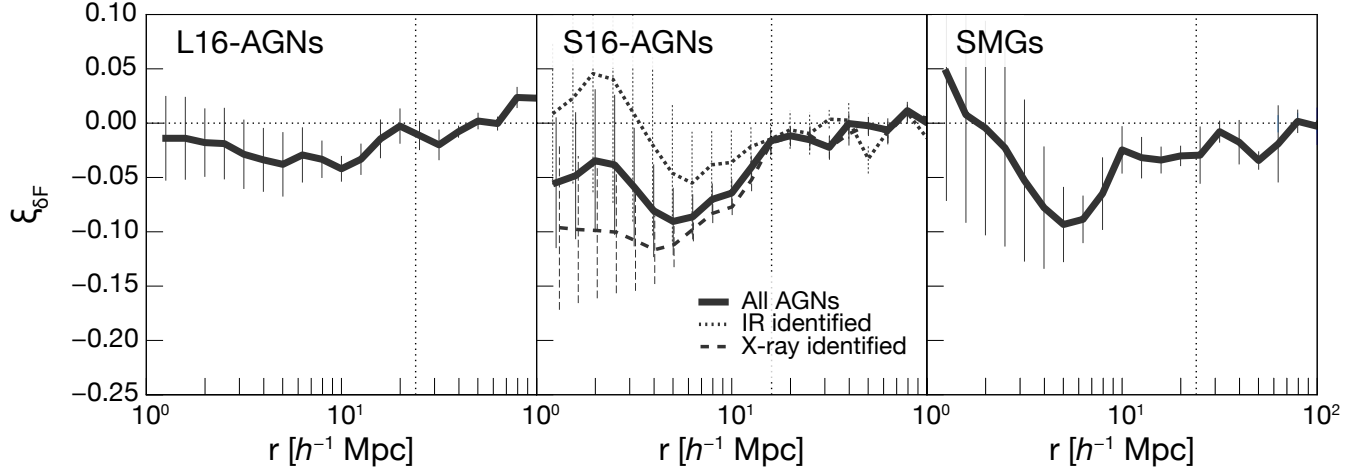


**Figure 10.** CCFs of L16-AGNs, S16-AGNs, and SMGs from left to right as a function of radius in comoving units. The meaning of vertical dotted lines is the same as in Figure 4.

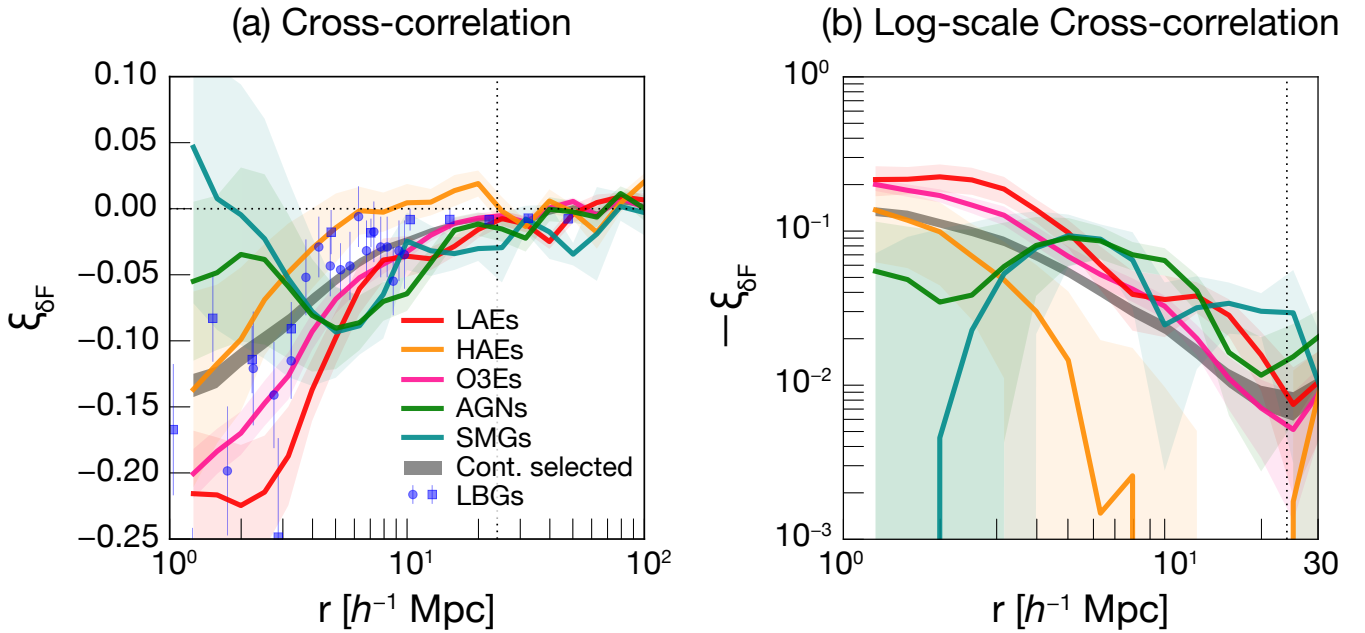


**Figure 11.** CCFs of different galaxy populations plotted on linear scale (a) and log scale (b) as a function of radius in comoving units. The CCF between Ly $\alpha$  absorption and LBGs from the literature is also plotted by blue circles (Adelberger et al. 2005) and squares (Bielby et al. 2017). The meaning of vertical dotted lines is the same as in Figure 4.

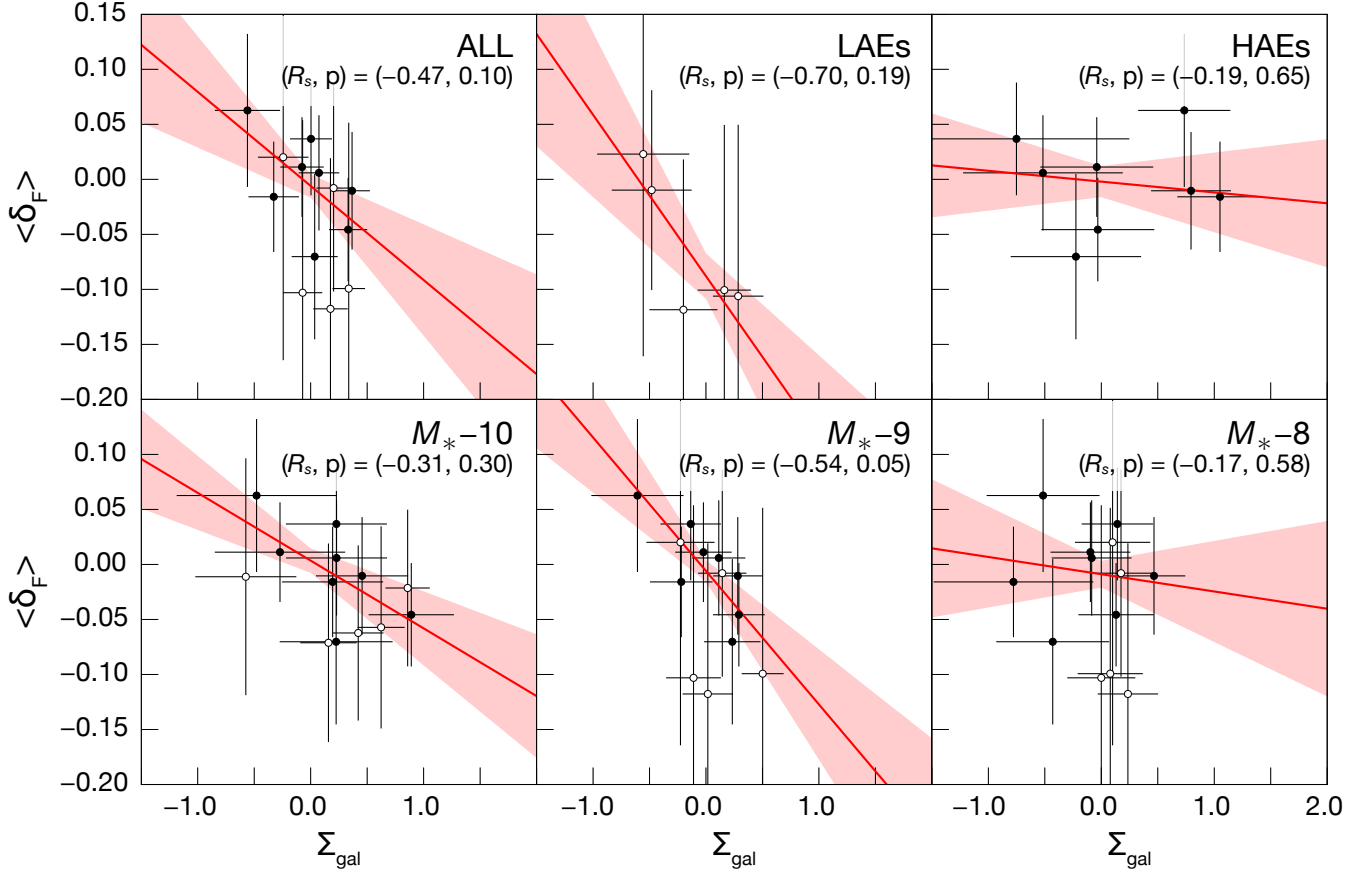


**Figure 12.**  $\langle \delta_F \rangle - \Sigma_{\text{gal}}$  relations obtained from local minima and maxima. Points colored in white and black are from  $2.14 < z < 2.22$  and  $2.215 < z < 2.247$  ranges, respectively. The best-fit linear models obtained from the combined two redshift ranges are shown by thick red lines with errors.

the subsamples with  $R_s = -0.17$  to  $-0.70$ . However, considering larger  $p$ -values ( $0.19 - 0.65$ ) except for the L16- $M_*-9$  and ALL, all the anti-correlations in Figure 12 are statistically insignificant. For the L16- $M_*-9$  and ALL, we obtain Spearman's coefficients of  $R_s = -0.54$  with the 95% confidence level and  $R_s = -0.47$  with the 90% confidence level, indicating the presence of weak anti-correlations. Likewise, Mukae et al. (2017) have also found an anti-correlation in their  $\langle \delta_F \rangle - \delta_{\text{gal}}$  relation evaluated from a cylinder that has a radius of  $r = 8.8 h^{-1}$  Mpc and the length of  $88 h^{-1}$  Mpc at  $z = 2.5$ , at a  $\sim 90\%$  confidence level with  $R_s = -0.39$ . The same analysis performed for all simulated galaxies in Momose et al. (2020) gives  $R_s = -0.37$  with the 98% confidence level, indicating a weak anti-correlation in the  $\langle \delta_F \rangle - \Sigma_{\text{gal}}$  relation.

We also apply  $\chi$ -square fitting to the  $\langle \delta_F \rangle - \Sigma_{\text{gal}}$  relations of all of our subsamples shown in Figure 12 with a linear model of

$$\langle \delta_F \rangle = \alpha + \beta \Sigma_{\text{gal}}. \quad (7)$$

The best-fit parameters are summarized in Table 3. Those of the two subsamples with a statistically confirmed anti-correlation are  $(\alpha = -0.006 \pm 0.010, \beta = -0.121 \pm 0.040)$  for L16- $M_*-9$  and  $(\alpha = -0.006 \pm 0.011, \beta = -0.085 \pm 0.040)$  for ALL. Mukae et al. (2017) have obtained  $\alpha = -0.17 \pm 0.06$  and  $\beta = -0.14^{+0.06}_{-0.16}$ . Momose et al. (2020) have also evaluated the best-fit linear model of  $\langle \delta_F \rangle - \Sigma_{\text{gal}}$  relations with the numerical simulations and found  $\alpha = -0.126 \pm 0.006$  and  $\beta = -0.018 \pm 0.006$ . The slopes  $\beta$  of L16- $M_*-9$  and ALL are consistent with the one by Mukae et al. (2017) within the errors but are much steeper than the one obtained from the simulations. As has already been discussed in Momose et al. (2020), such a discrepancy in slope between observations and simulations may be due to photo- $z$  errors. For example, the typical photo- $z$  error of L16 galaxies ( $\sigma_z = 0.07$ ) is larger than the thickness of the HAE slice ( $\Delta z = 0.032$ ), meaning that  $\Sigma_{\text{gal}}$  measurements have been contaminated from galaxies outside the slice. This smearing of  $\Sigma_{\text{gal}}$  would make an observed slope steeper than the true value.

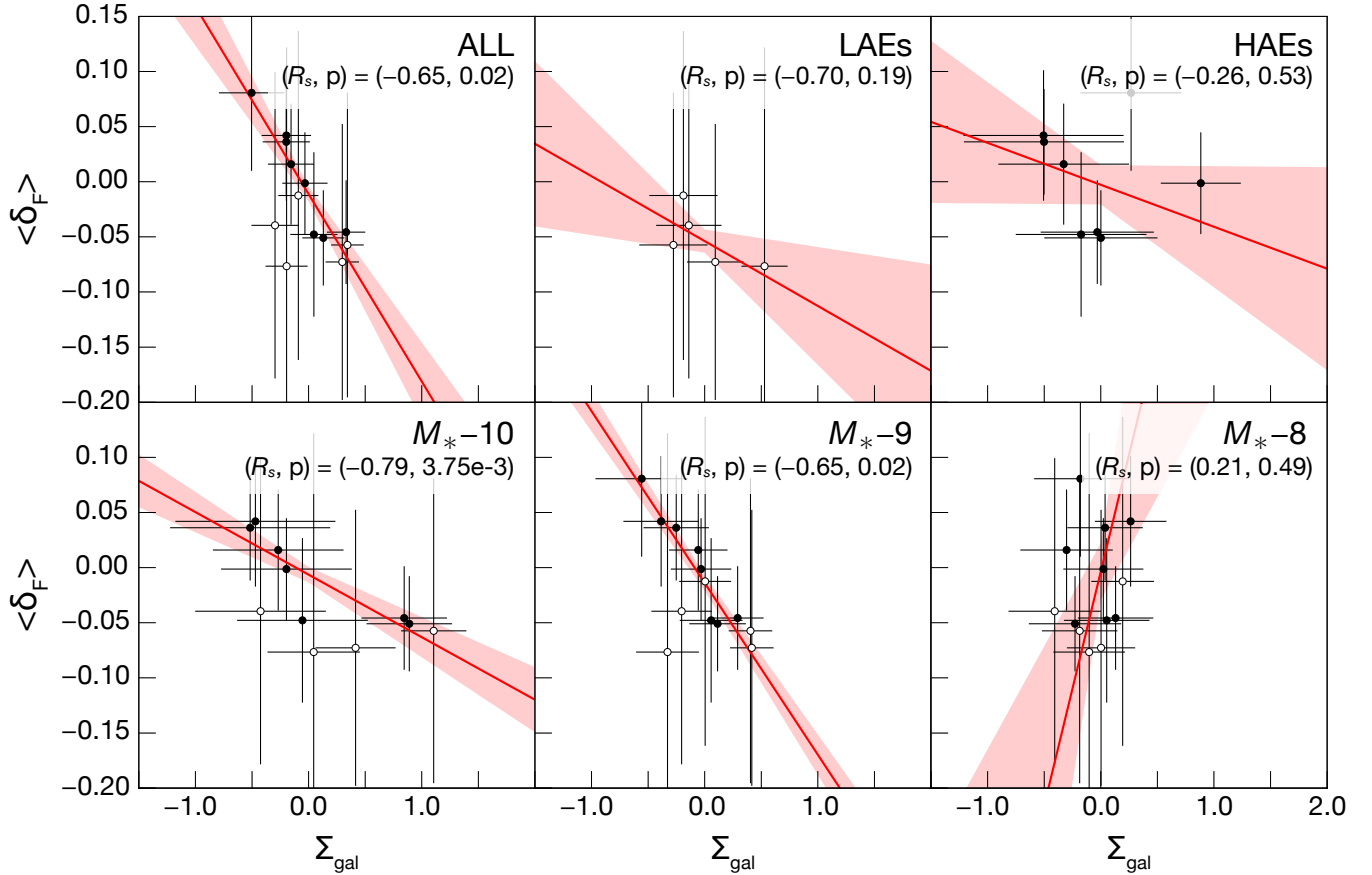


**Figure 13.** Same as Figure 12, but evaluated from random positions.

Since Mukae et al. (2017) have pointed out a possible bias in the  $\langle \delta_F \rangle - \Sigma_{\text{gal}}$  relation due to the position of sightlines, we also perform overdensity analysis based on randomly selected sightline positions. As shown in Figure 13 and Table 4, similar results are obtained for most of the subsamples. Statistically significant anticorrelations are confirmed only in L16- $M_* - 10$ , L16- $M_* - 9$ , and ALL with 98%, more than 99%, and 98% confidence levels respectively, which are also consistent with the literature (Mukae et al. 2017; Momose et al. 2020).

Separately from the significance of correlations, we also find intriguing results for LAEs. Although the error bars are large, the distribution of LAEs in  $\Sigma_{\text{gal}}$  seems to be slightly wider than those of L16- $M_* - 9$  and L16- $M_* - 8$  subsamples at  $2.14 < z < 2.22$  (white points in Figures 12 and 13). The width of the  $\Sigma_{\text{gal}}$  distribution is 0.84, 0.73, and 0.47 (0.80, 0.74, and 0.41) for LAEs, L16- $M_* - 9$ , and L16- $M_* - 8$  subsamples in Figure 12 (Figure 13). We will briefly discuss possible implications from the larger  $\Sigma_{\text{gal}}$  distribution in Section 5.2.3.

## 5. DISCUSSION

### 5.1. What Can We Find About the IGM-Galaxy Connection through the Two Approaches?

In this study, we adopt two methods to investigate the IGM-galaxy connection: one is cross-correlation analysis, and the other is overdensity analysis. These methods are sensitive to different aspects of the IGM-galaxy connection and have both strong and weak points.

#### 5.1.1. Cross-correlation Analysis

By measuring average HI overdensities as a function of distance, cross-correlation analysis tells us how a given galaxy population traces the cosmic HI web. The advantage of this method is that a CCF signal can be detected even for a small number of galaxies. Indeed, as shown in Section 4.1, we confirm a significant CCF signal for only seven HAEs and four SMGs.

Note, however, that a CCF from a small sample may be greatly different from the true one owing to large statistical errors (Momose et al. 2020). The irregular shapes seen in the CCFs of  $M_* - 11$ ,  $M_* - 8$ , SFR-(i), SFR-(iv), and sSFR-(iii) subsamples could be due to their small sample sizes. In contrast, the CCF obtained



from a sufficiently large number of randomly selected galaxies is close to the true one. It can be the case for the  $M_\star$ -9,  $M_\star$ -10, SFR-(ii), sSFR-(i), and SFG subsamples, which show consistent CCFs between L16 and S16. In addition, we can obtain a CCF similar to the true one even from a small sample, if galaxies of a given type reside in a similar gas environment. It may be the case for LAEs, HAEs, AGNs, and SMGs.

A disadvantage of cross-correlation analysis is that it requires spec- $z$  measurements. This is because the typical photo- $z$  error (i.e.,  $\sigma_z = 0.05 - 0.1$  at  $z \sim 2$  corresponding to  $40 - 90 h^{-1}$  Mpc, e.g., Muzzin et al. 2013; Laigle et al. 2016; Straatman et al. 2016) is much larger than the scales over which the cosmic HI density varies (a few Mpc scale). If galaxies with spec- $z$  measurements do not represent the parent sample, the CCF obtained from them may be biased in some manner.

### 5.1.2. Overdensity Analysis

The other method used in this study is overdensity analysis. An advantage of this method is that it can evaluate the tightness of the correlation between galaxy and IGM densities (the IGM-galaxy connection) for a given size of cells. If sufficiently long (along the line-of-sight) cells are adopted as in the case of this study ( $\Delta z = 0.08$  and  $0.032$ ), photo- $z$  samples can be used. A drawback of using such long cells is that the overdensities of galaxies and IGM for such cells are small and hence noisy. Owing to this disadvantage, combined with the fact that the sky coverage of the CLAMATO is not large enough to put many independent cells, we cannot confirm a  $\langle \delta_F \rangle - \Sigma_{\text{gal}}$  correlation with a high significance for several subsamples.

## 5.2. Implications for the IGM-Galaxy Connection of Each Galaxy Population

In this subsection, we discuss the IGM-galaxy connection depending on galaxy properties (i.e.,  $M_\star$ , SFR, and sSFR) and galaxy populations.

### 5.2.1. Nature of the Major Contributor to the CCF of Continuum-selected Galaxies

From Section 4.1.1, we find that galaxies with  $M_\star \sim 10^{10} M_\odot$  and  $\text{SFR} \sim 10 M_\odot \text{ yr}^{-1}$  are dominant and responsible for the CCF of continuum-selected galaxies. In fact, the number histograms of  $M_\star$  for the L16 and S16 samples shown by gray shades in Figure 14 have a peak at around  $M_\star \sim 10^{10} M_\odot$ . On the other hand, the comparison with Momose et al. (2020) in Figure 6 shows that the CCF of continuum-selected galaxies is reproduced by the  $M_\star$ -9, SFR-(iii), SFR-(iv), and sSFR-(ii) subsamples, implying that continuum-selected galaxies have  $M_\star \sim 10^9 M_\odot$  and  $\text{SFR} \sim 0.1 - 1 M_\odot \text{ yr}^{-1}$  (see

also Section 4.1.2). These small discrepancies in  $M_\star$  and SFR between the observed and simulated galaxies, if real, may be due to differences in galaxy models used in SED fitting between the L16/S16 samples and the simulations. Unfortunately, however, we cannot identify the cause at this point, because the volume covered by the CLAMATO is still insufficient. Future surveys for 3D tomography, such as the one by the Prime Focus Spectrograph (PFS) on the Subaru Telescope, will enable us to investigate it in detail.

### 5.2.2. Reasons for the Lack of CCF Variation in $M_\star$ , SFR, and sSFR Subsamples

Although Momose et al. (2020) have found a clear dependence of the CCF on  $M_\star$  and SFR, we do not find such significant dependence in this study (see Section 4.1.1). We also do not find any clear dependence on galactic properties, even though we divide the galaxy sample into two (see Appendix B). We give two possible reasons in the following.

First is the small sample size used in our observational analysis. Momose et al. (2020) have demonstrated that a small randomly selected sample cannot always reproduce the true CCF. As we have already described in Section 5.1, such a small sample size can cause an irregular CCF like those of several subsamples in Figure 5.

The second possible reason is the errors in stellar mass and SFR estimates for the L16 and S16 samples. Fainter galaxies have more chance to be assigned to wrong subsamples owing to larger photometric errors. Furthermore, L16 and S16 use different SED models, implying that galaxies with the same SED measurements can even be assigned to different subsamples. Smaller subsamples will suffer more from such misclassification because of heavier contaminations from other subsamples. Indeed, the subsamples that give consistent CCFs between L16 and S16 have relatively large sizes. In order to examine whether or not the mass and SFR dependence of the CCF found in Momose et al. (2020) exist in the real observational data, we need a larger galaxy sample and/or a larger 3D tomography volume.

### 5.2.3. LAEs

In Section 4.1.3, we show that the LAEs have the strongest CCF signal among all the subsamples at  $r < a \text{ few } h^{-1} \text{ Mpc}$ . In Section 4.2, we also tentatively find that the LAEs have a slightly wider  $\Sigma_{\text{gal}}$  distribution than the  $M_\star$ -9 and  $M_\star$ -8 subsamples, which are comparable in stellar mass to LAEs (e.g., Hagen et al. 2014, 2016; Shimakawa et al. 2017a; Kusakabe et al. 2018; Khostovan et al. 2019, see also Figure 14). These results suggest that on both small and large-scales, LAEs

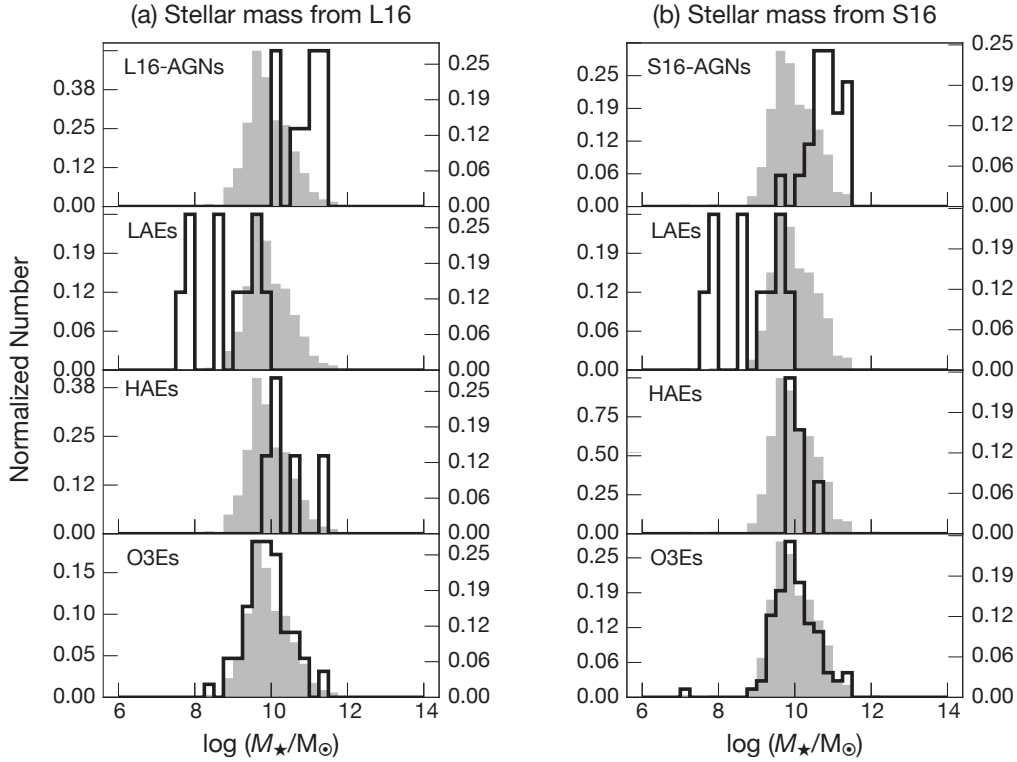


**Figure 14.** Normalized number histograms of galaxies as a function of stellar mass ( $M_*$ ). The solid black line indicates the histogram of each galaxy population – AGNs, LAEs, HAEs, and O3Es from top to bottom. The histograms of the L16 and S16 spec- $z$  samples are overlaid by gray shades in panels (a) and (b) for comparison. The normalized numbers of each galaxy population and L16/S16 are shown on the left and right axes, respectively. Note that we only plot galaxies with  $M_*$  estimates.

tend to be located in higher IGM density regions than galaxies with comparably low stellar masses. However, our LAEs seem to favor lower stellar masses on average than the other line emitters as shown in Figure 14<sup>3</sup>. The result that LAEs tend to be found in high IGM density regions despite their low masses apparently conflicts with the hierarchical structure formation model. Although we have not been able to resolve this conflict, we offer two possible explanations below. One is that regions where LAEs exist are those with low matter densities but with high HI fractions. Indeed, the IGM HI fraction can vary depending on the presence or absence of strong radiative sources such as starbursts and AGNs (e.g., Umehata et al. 2019; Mukae et al. 2020). It is, however, not clear whether this explanation can also be compatible with the result that the LAEs have the strongest CCF signal among all the galaxy popula-

tions. Another possibility may be that LAEs are satellite galaxies associated with massive halos, although this possibility is apparently incompatible with the observed weak clustering of LAEs at  $z = 2 - 3$  (e.g., Guaita et al. 2010; Kusakabe et al. 2018). Therefore, this strongest CCF signal of LAEs is puzzling because both the stellar-mass divided subsamples in this paper discussed below and Momose et al. (2020) show that lower-mass galaxies correlate more weakly with the IGM.

Another intriguing feature of the LAEs’ CCF is its shape, which shows a flat profile until  $r \sim 3 h^{-1}$  Mpc. We find that such a profile cannot be reproduced unless most LAEs are located not in an HI density peak but  $2 - 3 h^{-1}$  Mpc away from it. Indeed, such a situation is evident in the postage stamps of LAEs (Figure 15 in Appendix A). That is to say, LAEs may not faithfully trace the underlying cosmic web.

When the six subsamples selected on LAE properties are considered (see Figure 8), we find another interesting trend: that LAEs with faint  $L_{\text{Ly}\alpha}$ , small  $EW_{\text{Ly}\alpha}$ , and bright  $L_{\text{UV}}$  have a higher signal than their counterparts with opposite properties. We argue that its origin is possibly a mass-dependent IGM–galaxy correlation. Momose et al. (2020) have found that more

<sup>3</sup> We derive  $M_*$  values for LAEs with Spitzer/IRAC photometry by SED fitting in a similar manner to that used in Kusakabe et al. (2015, 2018). The stellar masses of AGNs, HAEs, and O3Es are taken from L16 and S16. Note that not all galaxies have  $M_*$  measurements. Thus, we only plot galaxies with  $M_*$  measurements in Figure 14.

massive galaxies have a higher CCF signal. This result, combined with the fact that LAEs with a smaller  $EW_{\text{Ly}\alpha}$  and a brighter  $L_{\text{UV}}$  tend to be more massive (e.g., [Khostovan et al. 2019](#); [Kusakabe et al. 2019](#)) is qualitatively consistent with the trend found in Figure 8. Note, however, that this explanation is apparently inconsistent with the result that the CCF of LAEs is higher than that of continuum-selected galaxies with similar  $M_*$ . On the other hand, LAEs with large  $EW_{\text{Ly}\alpha}$  and faint  $L_{\text{UV}}$  show a similar CCF profile to that of continuum-selected galaxies. It may indicate that less massive LAEs trace the IGM distribution in a similar manner to continuum-selected galaxies.

We also discuss a possible contribution of AGNs in our LAE sample based on  $L_{\text{Ly}\alpha}$ -dependent CCFs. Some observations have suggested that the AGN fraction is close to unity at  $L_{\text{Ly}\alpha} \geq 10^{43} \text{ erg s}^{-1}$  (e.g., [Konno et al. 2016](#); [Sobral et al. 2018](#)). Although our LAEs do not have any clear AGN signatures, contamination by hidden AGNs cannot be ruled out. Given that AGNs are hosted by more massive dark matter halos than LAEs, they should show a stronger CCF signal than LAEs, and may have a similar CCF to our AGNs and SMGs (see also Section 5.2.6). However, because our  $L_{\text{Ly}\alpha}$ -luminous subsample does not have either a stronger CCF signal or a similar CCF profile to those of AGNs and SMGs in Figure 10, the influence of hidden AGNs may be negligible.

Another interesting feature seen in Figure 8 is that LAEs with faint  $L_{\text{Ly}\alpha}$  and small  $EW_{\text{Ly}\alpha}$  have a flat CCF profile. If the  $\text{Ly}\alpha$  emission from LAEs is suppressed by HI in the surrounding IGM ([Gunn & Peterson 1965](#); [Haiman 2002](#); [Santos 2004](#); [Dijkstra et al. 2007](#)), LAEs in dense environments must have faint  $L_{\text{Ly}\alpha}$  and/or small  $EW_{\text{Ly}\alpha}$ . Previous observational studies have suggested a possible reduction of the  $\text{Ly}\alpha$  escape fraction of galaxies in high-density regions due to high IGM densities (e.g., [Toshikawa et al. 2016](#); [Shimakawa et al. 2017b](#); [Ao et al. 2017](#)). Therefore, the flat profiles seen in Figure 8 may suggest that LAEs in density peaks of the IGM cannot be detected, and thus only LAEs off the peaks where the HI density is not very high are detected.

#### 5.2.4. HAEs

In Figure 7, we find that the CCF of HAEs is comparable to that of the continuum-selected galaxies. It indicates that these two populations trace the IGM in a similar manner. The consistency of their CCFs is naturally explained by the fact that the normalized number histogram of  $M_*$  for our HAEs has a peak at  $M_* \sim 10^{10} M_\odot$  (see Figure 14), which is in the expected mass range of the continuum-selected galaxies.

#### 5.2.5. O3Es

Because our O3Es have a similar  $M_*$  distribution to those of L16/S16 as found in Figure 14, they are expected to have a similar CCF to those of the continuum-selected galaxies and HAEs. Nonetheless, they have a stronger signal than the continuum-selected galaxies and HAEs as shown in Figure 7, suggesting that they reside in higher-density regions. Thus, our O3Es might be biased toward higher halo masses.

Further cross-correlation analyses to examine  $L_{[\text{OIII}]\lambda\lambda 5007}$  and  $EW_{[\text{OIII}]\lambda\lambda 5007}$  dependence in Figure 9 show no significant trend between the CCF signal and  $L_{[\text{OIII}]\lambda\lambda 5007}$  or  $EW_{[\text{OIII}]\lambda\lambda 5007}$ . This implies that the IGM–O3Es connection is generally independent of their properties. However, because there exists a positive correlation between  $L_{[\text{OIII}]}$  of O3Es and hosting dark halo mass ([Khostovan et al. 2018](#)), the highest CCF signal in the  $EW_{[\text{OIII}]\lambda\lambda 5007} \geq 300 \text{ \AA}$  subsample perhaps indicates that only massive O3Es strongly connect to high-density HI.

#### 5.2.6. AGNs and SMGs

The CCFs of AGNs and SMGs have very different shapes from that of star-forming galaxies. Although it is unclear in L16-AGNs (Figure 10 left), the CCF takes the minimum value not at the center but at  $r = 5 - 6 h^{-1} \text{ Mpc}$  in both AGNs and SMGs, indicating that they are typically distributed  $5 - 6 h^{-1} \text{ Mpc}$  away from HI density peaks. Indeed, we confirm that they are mainly found at the outskirts of the cosmic web in Figure 15.

If AGNs and SMGs represent massive galaxies with  $M_{\text{DH}} = 10^{11} - 10^{13} M_\odot$  (e.g., [Myers et al. 2007](#); [Weiß et al. 2009](#); [Allevato et al. 2011, 2012, 2014, 2019](#); [Hickox et al. 2012](#); [Koutoulidis et al. 2013](#); [Plionis et al. 2018](#); [Suh et al. 2019](#)), they should be found in high IGM density regions on average. However, the average HI density around them is not so high and is in some cases even lower than the cosmic mean. It implies HI depletion in several comoving Mpc around them. Because a half of our SMGs are also confirmed as AGNs, such HI depletion is likely caused by the IGM HI photoionization, which is called the proximity effect. [Mukae et al. \(2020\)](#) have also suggested that the off-center peak of their mean  $\delta_{\text{F}}$  measurements around QSOs is due to the proximity effect. QSOs at  $z = 2 - 3$  have proximity zones of  $r = 2 - 10 h^{-1} \text{ Mpc}$  (e.g., [D’Odorico et al. 2008](#); [Uchiyama et al. 2019](#)), which is consistent with the peak radii of AGNs’ and SMGs’ CCFs, thus supporting our interpretation.

The shape and the peak positions of the CCFs also likely depend on AGN type as we already present in Section 4.1.3. We find that IR-identified (*X*-ray-identified) AGNs show positive (negative)  $\xi_{\delta\text{F}}$  values at the cen-

ter. This suggests that IR-identified AGNs are in HI underdense regions, but  $X$ -ray-identified AGNs are still in overdense regions. Such different environments depending on AGN type are possibly determined by the balance between the baryon accretion rate (mainly gas) to the host galaxy and the IGM HI photoionization rate. If the former is higher (lower) than the latter, the HI around the galaxy can become overdense (underdense).

Obscured AGNs, including SMGs and IR-identified AGNs, are generally hosted by starburst-like and/or young galaxies (e.g., Hatziminaoglou et al. 2010; Ichikawa et al. 2012). On the contrary,  $X$ -ray-identified AGNs, often denoted as Type 1 or unobscured AGNs, are suggested to be hosted by more massive halos of  $M_{\text{DH}} = 10^{12} - 10^{13} M_{\odot}$  than obscured AGNs (Allevalo et al. 2014; Suh et al. 2019). Because the accretion rate is proportional to the halo mass (Dekel et al. 2013), the accretion rate of  $X$ -ray-identified AGNs is perhaps higher than the photoionization rate, and thus their surrounding IGM becomes overdense. On the other hand, some studies have shown that Type 2 or obscured AGNs might have a higher Eddington ratio than Type 1 AGNs at the same bolometric luminosity, implying relatively higher photoionization rates (e.g., Lusso et al. 2012). If this is the case for our IR-identified AGNs and SMGs, and their accretion rates are not high enough to exceed the photoionization rate, they would ionize the surrounding HI and make HI underdense environments.

### 5.3. Comparison of the IGM–Galaxy Connection among Galaxy Populations

Figure 11 shows that the CCF varies among the galaxy populations. In addition, the population with the strongest CCF signal is different depending on scale (i.e., large or small). For large scales over  $r \geq 5 h^{-1}$  Mpc, AGNs and SMGs have the highest CCF signal among all the populations. Momose et al. (2020) have shown that the higher a galaxy stellar/halo mass is, the stronger a CCF signal is. In fact, our AGNs are clearly in the higher- $M_{\star}$  regime than the other galaxy populations (Figure 14). In addition, both AGNs and SMGs are known to be hosted by massive halos ( $M_{\text{DH}} = 10^{11} - 10^{13} M_{\odot}$ ; e.g., Weiß et al. 2009; Allevalo et al. 2011, 2012, 2014, 2019; Hickox et al. 2012; Koutoulidis et al. 2013; Plionis et al. 2018; Suh et al. 2019). Hence, their highest CCF signal is reasonable.

Interestingly, AGNs and SMGs are not in high-density regions at small scales within  $r = 4 - 5 h^{-1}$  Mpc. We argue that it is due to their proximity effect (see also Section 5.2.6). Instead, LAEs show the highest CCF signal among all the populations at small scales, suggesting that they are in the densest HI regions. This result is

apparently inconsistent with the fact that LAEs are typically hosted by low-mass halos ( $M_{\text{DH}} = 10^{10} - 10^{11} M_{\odot}$ , e.g., Guaita et al. 2011; Kusakabe et al. 2018; Khostovan et al. 2019). This inconsistency is also confirmed in the number histogram of  $M_{\star}$  in Figure 14, showing that LAEs are biased toward lower  $M_{\star}$  than the other line emitters. In order to identify the reason why LAEs are in higher IGM density regions than the other galaxy populations on small scales, more investigations based on larger galaxy samples are essential.

Another feature of the CCF worth comparing among all the galaxy populations is its shape. If a given galaxy population faithfully traces the underlying HI density structure, its CCF should increase toward the cosmic mean ( $\xi_{\delta\text{F}} = 0$ ) monotonically. All star-forming galaxies except LAEs show such CCFs (Figure 11). However, LAEs have a flat CCF shape up to  $r \sim 3 h^{-1}$  Mpc, suggesting that they are in a few  $h^{-1}$  Mpc away from peaks of the cosmic web. This means that overdense regions traced by LAEs do not agree with those traced by other star-forming galaxies. Such a discordance has also been reported in the literature (e.g., Shimakawa et al. 2017b; Shi et al. 2019). It may be due to the attenuation of Ly $\alpha$  emission by abundant HI at the peaks of cosmic web.

### 5.4. Possible Relation between Galaxies and IGM in Terms of Galaxy Evolution

Finally, we discuss how galaxies correlate with the IGM in terms of their evolution by combining all of our results and discussion. After their birth, galaxies acquire gas from intergalactic space and stay in the main-sequence while they form stars. During this period, the CCF on both large and small scales is determined by the host halo mass of galaxies, as is also indicated in Momose et al. (2020). According to the theoretical framework of galaxy evolution (e.g., Hopkins et al. 2008), massive galaxies experience the AGN/QSO phase. When the AGN activity becomes prominent, galaxies radiate strong ionizing photons and generate a Mpc-scale proximity region, thus suppressing the CCF on small scales as seen for our AGNs and SMGs. However, because AGNs and SMGs are generally hosted by more massive halos than star-forming galaxies, the total gas density around them on large scales will be higher, as confirmed for our AGNs and SMGs. After the AGN and/or QSO phase, galaxies become gradually senescent and quiescent owing to the quenched star formation (e.g., Hopkins et al. 2008). The Mpc-scale IGM HI environments may be determined by the balance between accretion rate and HI photoionization rate in the IGM as we discussed in Section 5.2.6. Because such galaxies are generally hosted by more massive halos, the large-scale HI den-

sity would be possibly high, and even higher than those of AGNs and SMGs. However, we cannot verify the hypothesis from current observational data owing to the lack of large quiescent galaxy samples. We leave further investigations for our future work.

## 6. SUMMARY

In this study, we investigate the IGM–galaxy connection, paying attention to its dependence on galactic properties, such as  $M_*$ , SFR, sSFR, and their populations. Using the publicly available 3D  $\text{Ly}\alpha$  absorption tomography data CLAMATO (Lee et al. 2016, 2018), and several galaxy catalogs in the literature, we measure the CCF between IGM HI and galaxies and examine the correlation between  $\langle\delta_{\text{F}}\rangle$  and galaxy number density  $\Sigma_{\text{gal}}$ . The results of this study are summarized below.

1. We detect a CCF signal up to  $r \sim 50 h^{-1}$  Mpc from the continuum-selected galaxies (Figure 4). We compare it with those of  $M_*$ , SFR, and sSFR subsamples of simulated galaxies in Momose et al. (2020), and find that the results of  $M_*$ -9, SFR-(iii), SFR-(iv), and sSFR-(ii) subsamples agree with the observed one over  $r = 3 - 20 h^{-1}$  Mpc (Figure 6). In contrast, within the observed galaxies, the CCF of the continuum-selected galaxies agrees with the  $M_*$ -9,  $M_*$ -10, SFR-(ii), SFR-(iii), and sSFR-(i) subsamples. These small discrepancies between the observed and simulated galaxies may be attributed to differences in SED models used in the photo- $z$  catalogs (i.e., L16 and S16) and Momose et al. (2020).
2. We divide the continuum-selected galaxies into two to four subsamples based on  $M_*$ , SFR, sSFR, and galaxy type (either SFG or QG) measurements given in L16 and S16 and calculate cross-correlations (Figure 5). Between L16 and S16, we confirm the consistency of CCFs only in the  $M_*$ -9,  $M_*$ -10, SFR-(ii), sSFR-(i), and SFG subsamples. In addition, we do not confirm the  $M_*$ , SFR, and sSFR dependence on the CCF that is found by Momose et al. (2020) for simulated galaxies. We suggest that the lack of CCF trends could be a result of a combination of 1) small sample sizes and 2) random and systematic errors in  $M_*$  and SFR estimates.
3. We calculate CCFs for LAEs, HAEs, O3Es, AGNs, and SMGs and obtain the following results.
  - **LAEs:** LAEs are found to have the strongest CCF signal at the center, and hence reside

in the highest-density regions, among all the galaxy populations examined in this study (Figure 11). We also find that LAEs with faint  $L_{\text{Ly}\alpha}$ , small  $EW_{\text{Ly}\alpha}$ , and bright  $L_{\text{UV}}$  have a stronger CCF signal (Figure 8). We also find the CCF is flat up to  $r = 3 h^{-1}$  Mpc. It probably reflects the fact that LAEs do not reside in the density peaks of the IGM, but a few Mpc away from them. Such offsets may be due to the attenuation of  $\text{Ly}\alpha$  emission by abundant HI in high-density regions of the cosmic web.

- **HAEs:** The CCF of HAEs is comparable to that of continuum-selected galaxies (Figure 7). It indicates that these two populations trace the IGM in a similar manner because of similar stellar masses.
  - **O3Es:** Although we expect similar CCF strengths between HAEs and O3Es considering their comparable stellar masses, the latter have a higher CCF (Figure 7). Because our O3Es with spec- $z$  measurements are biased toward higher [OIII]  $\lambda\lambda 5007$  luminosities, they may be biased toward higher stellar (and hosting halo) masses.
  - **AGNs & SMGs:** AGNs and SMGs commonly have a negative peak at  $r \sim 5 h^{-1}$  Mpc (Figure 10), implying that they tend to be in locally low-density regions. Considering that a half of our SMGs are also confirmed as AGNs, such HI depletion may be due to the proximity effect. We also find a hint that the CCF of IR ( $X$ -ray) identified AGNs is weaker (stronger) at the center. This difference may imply that IR identified AGNs have higher photoionization rates.
4. On large scales ( $r \geq 5 h^{-1}$  Mpc), AGNs and SMGs have the highest CCF amplitude among all the populations. This is reasonable because they are generally hosted by the most massive halos with  $M_{\text{DH}} = 10^{11} - 10^{13} M_{\odot}$ . On small scales ( $r < 5 h^{-1}$  Mpc), on the other hand, LAEs show the highest signal. However, the cause of such a high signal in LAEs, which are typically hosted by low-mass halos, is still unclear (see Figure 11).
  5. We examine the correlation between  $\langle\delta_{\text{F}}\rangle$  and  $\Sigma_{\text{gal}}$  (“overdensity analysis”; see Figures 12 and 13). We only confirm statistically significant anti-correlations in the L16- $M_*$ -9 and ALL subsamples. Their slopes are comparable to that in the

literature but steeper than those found in Momose et al. (2020), probably due to photo- $z$  errors. We also tentatively find that LAEs have a slightly wider  $\Sigma_{\text{gal}}$  distribution than the L16- $M_{\star}$ -9 and L16- $M_{\star}$ -8 subsamples at the same redshift slice, which are comparable in stellar mass to LAEs. It may suggest that LAEs have a stronger correlation with the IGM HI for their stellar masses.

#### ACKNOWLEDGEMENTS

We appreciate the anonymous referee for careful reviewing and useful comments that improved our paper. We are grateful to Dr. K.-G. Lee for providing the CLAMATO data and Dr. D. Sobral for providing the mask data of Sobral et al. (2013b). We thank Drs. M. Rauch, F. S. Zahedy, K. Ichikawa, T. Kawamuro,

M. Imanishi, H. Yajima, D. Sorini, T. Suarez Noguez, K. Kakiichi, and R. A. Meyer for helpful discussions. R.M. acknowledges a Japan Society for the Promotion of Science (JSPS) Fellowship at Japan. This work is supported by the JSPS KAKENHI grant Nos. JP18J40088 (RM), JP19K03924 (KS), and JP17H01111, 19H05810 (KN). The Laigle et al. (2016) galaxy catalog is based on data products from observations made with ESO Telescopes at the La Silla Paranal Observatory under ESO program ID 179.A-2005 and on data products produced by TERAPIX and the Cambridge Astronomy Survey Unit on behalf of the UltraVISTA consortium. We acknowledge the Python programming language and its packages of numpy, matplotlib, scipy, and astropy (Astropy Collaboration et al. 2013).

#### APPENDIX

##### A. $\langle \Delta_F \rangle$ MAPS

In order to visualize the IGM HI density fluctuations around galaxies used in the CCF analysis, we make postage stamp images of the projected HI density distribution by collapsing a thin ( $\Delta z = 2 h^{-1}$  Mpc) CLAMATO cube centered at each galaxy. Selected examples of each galaxy population are shown in Figure 15. The galaxy position on the sky is marked by a white star.

##### B. MASS, SFR, SSFR DEPENDENCE ON THE CCFs

We find no significant dependence of the CCF on galactic properties in Section 4.1.1 and Figure 5, in contrast to what Momose et al. (2020) have found for simulated galaxies. This lack of dependence could have resulted from large statistical uncertainties owing to the small sample sizes. To reduce the statistical uncertainties, we also perform a similar analysis by splitting L16 and S16 into only two subsamples by  $M_{\star}$ , SFR, and sSFR (Figure 16). Note that we use  $M_{\star} = 10^{10} M_{\odot}$ , SFR =  $10^1 M_{\odot} \text{ yr}^{-1}$ , and sSFR =  $10^{-9} \text{ yr}^{-1}$  as the border. We find that, for both L16 and S16, the higher-SFR subsample has a higher CCF at the  $2\sigma$  significance level up to  $r \sim 6 h^{-1}$  Mpc. Although it is in qualitative agreement with the trend found in Momose et al. (2020), the statistical significance may not be high enough to confirm the trend. On the other hand, no significant (or consistent) dependence is found on either  $M_{\star}$  or sSFR. A more precise analysis requires much larger galaxy samples in each category.

#### REFERENCES

- Adelberger, K. L., Shapley, A. E., Steidel, C. C., et al. 2005, ApJ, 629, 636, doi: [10.1086/431753](https://doi.org/10.1086/431753)
- Adelberger, K. L., Steidel, C. C., Shapley, A. E., & Pettini, M. 2003, ApJ, 584, 45, doi: [10.1086/345660](https://doi.org/10.1086/345660)
- Allevato, V., Finoguenov, A., Cappelluti, N., et al. 2011, ApJ, 736, 99, doi: [10.1088/0004-637X/736/2/99](https://doi.org/10.1088/0004-637X/736/2/99)
- Allevato, V., Finoguenov, A., Hasinger, G., et al. 2012, ApJ, 758, 47, doi: [10.1088/0004-637X/758/1/47](https://doi.org/10.1088/0004-637X/758/1/47)
- Allevato, V., Finoguenov, A., Civano, F., et al. 2014, ApJ, 796, 4, doi: [10.1088/0004-637X/796/1/4](https://doi.org/10.1088/0004-637X/796/1/4)
- Allevato, V., Viitanen, A., Finoguenov, A., et al. 2019, arXiv e-prints, arXiv:1910.08084, <https://arxiv.org/abs/1910.08084>
- Alonso, D., Colosimo, J., Font-Ribera, A., & Slosar, A. 2018, JCAP, 2018, 053, doi: [10.1088/1475-7516/2018/04/053](https://doi.org/10.1088/1475-7516/2018/04/053)
- Ao, Y., Matsuda, Y., Henkel, C., et al. 2017, ApJ, 850, 178, doi: [10.3847/1538-4357/aa960f](https://doi.org/10.3847/1538-4357/aa960f)
- Arnouts, S., Moscardini, L., Vanzella, E., et al. 2002, MNRAS, 329, 355, doi: [10.1046/j.1365-8711.2002.04988.x](https://doi.org/10.1046/j.1365-8711.2002.04988.x)

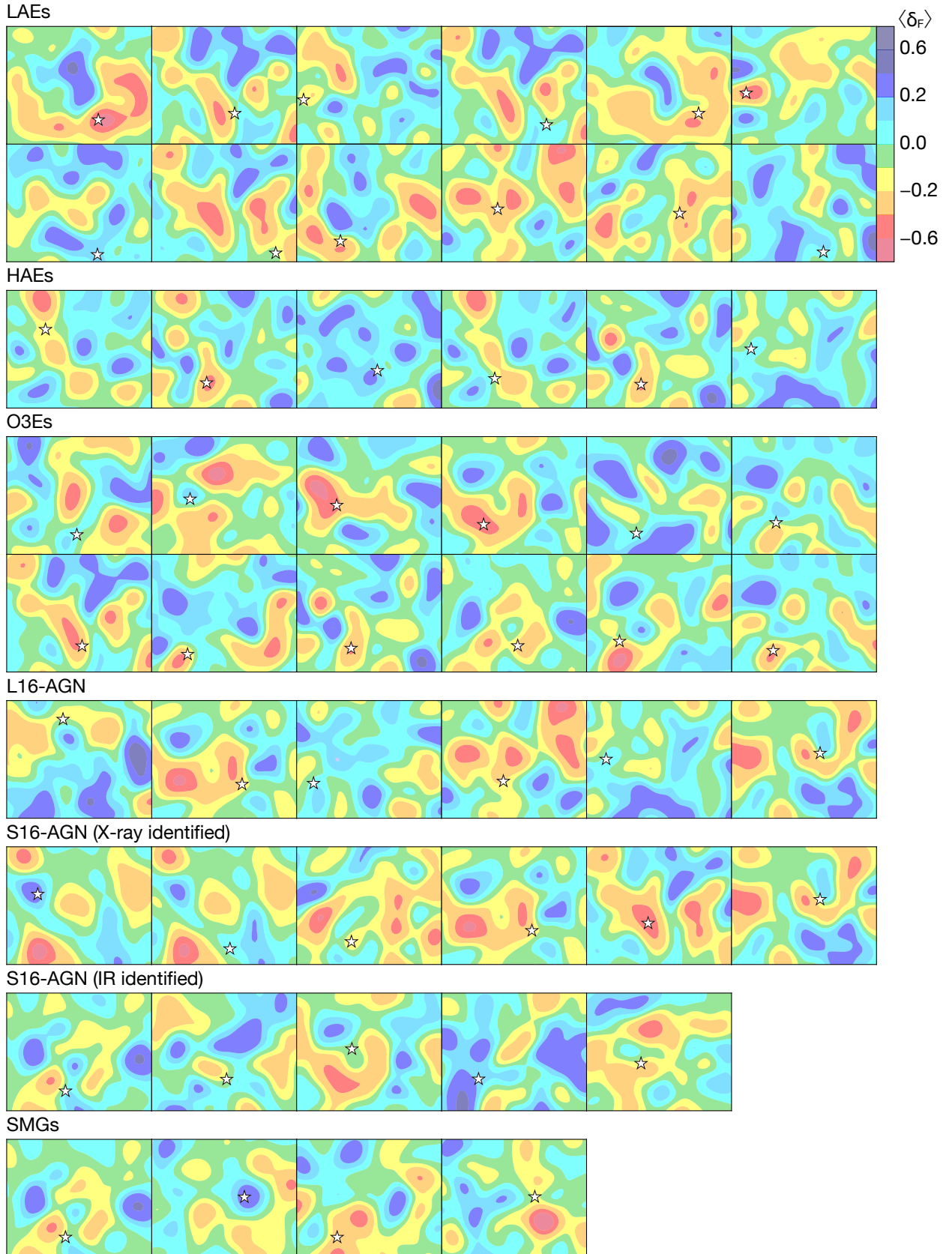


**Figure 15.** Projected HI density maps ( $30 h^{-1} \text{ Mpc} \times 24 h^{-1} \text{ Mpc}$ ) for randomly selected galaxies from each subsample, obtained by collapsing thin ( $\Delta z = 2 h^{-1} \text{ Mpc}$ ) data cubes around them. Open stars indicate the position of galaxies. Warm and cold colors denote overdense and underdense regions, respectively. Density maps of LAEs, HAEs and O3Es are arranged in the order of line luminosity from left to right, spanning two rows in the cases of LAEs and O3Es.

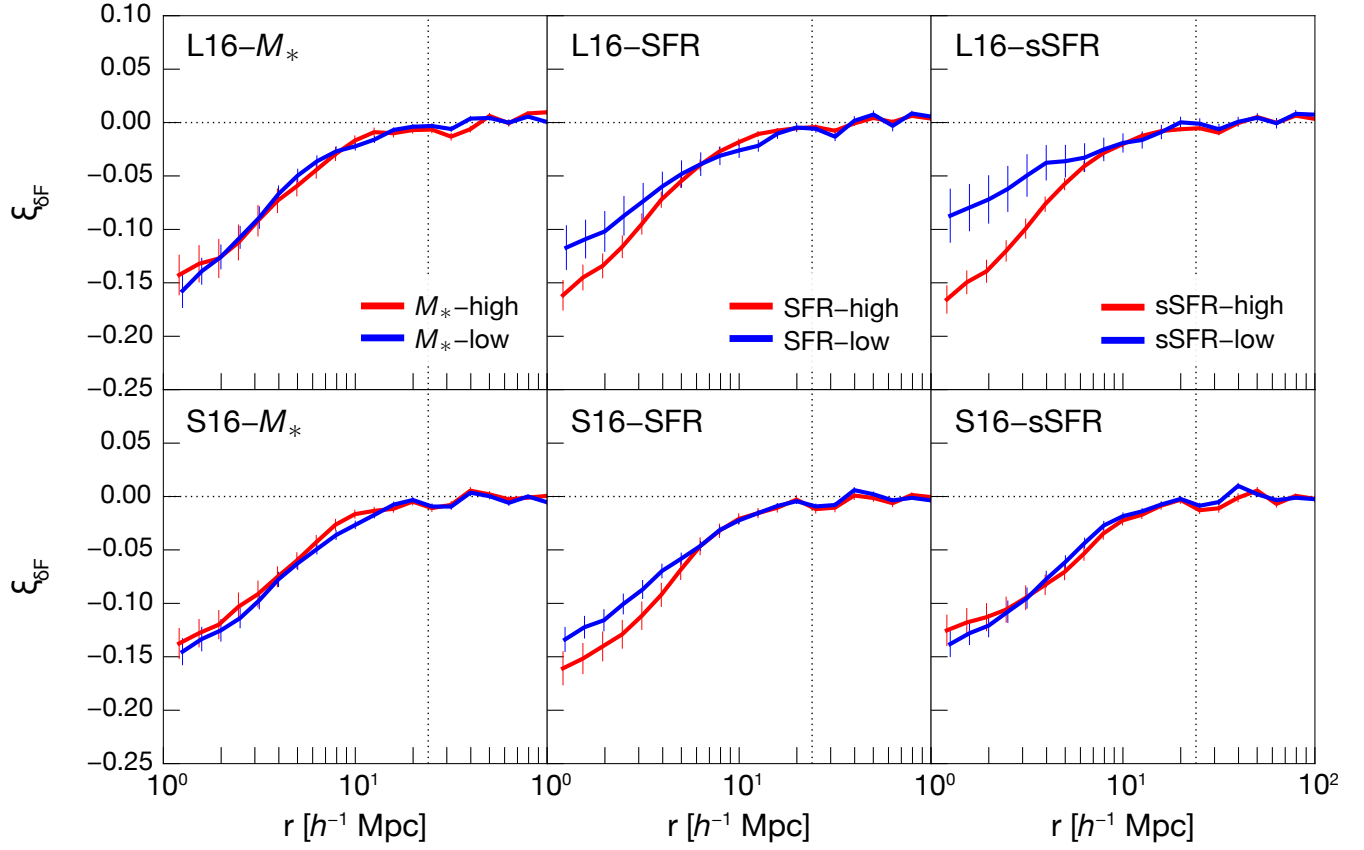


**Figure 16.** CCFs of (top) L16 and (bottom) S16 subsample pairs divided by  $M_*$ , SFR, and sSFR from left to right as a function of radius in comoving units. The meaning of vertical dotted lines is the same as in Figure 4.



- Astropy Collaboration, Robitaille, T. P., Tollerud, E. J., et al. 2013, *A&A*, 558, A33, doi: [10.1051/0004-6361/201322068](https://doi.org/10.1051/0004-6361/201322068)
- Balogh, M. L., McGee, S. L., Mok, A., et al. 2014, *MNRAS*, 443, 2679, doi: [10.1093/mnras/stu1332](https://doi.org/10.1093/mnras/stu1332)
- Bielby, R. M., Shanks, T., Crighton, N. H. M., et al. 2017, *MNRAS*, 471, 2174, doi: [10.1093/mnras/stx1772](https://doi.org/10.1093/mnras/stx1772)
- Brammer, G. B., van Dokkum, P. G., & Coppi, P. 2008, *ApJ*, 686, 1503, doi: [10.1086/591786](https://doi.org/10.1086/591786)
- Brisbin, D., Miettinen, O., Aravena, M., et al. 2017, *A&A*, 608, A15, doi: [10.1051/0004-6361/201730558](https://doi.org/10.1051/0004-6361/201730558)
- Cai, Z., Fan, X., Peirani, S., et al. 2016, *ApJ*, 833, 135, doi: [10.3847/1538-4357/833/2/135](https://doi.org/10.3847/1538-4357/833/2/135)
- Chabrier, G. 2003, *ApJL*, 586, L133, doi: [10.1086/374879](https://doi.org/10.1086/374879)
- Chen, H.-W., & Mulchaey, J. S. 2009, *ApJ*, 701, 1219, doi: [10.1088/0004-637X/701/2/1219](https://doi.org/10.1088/0004-637X/701/2/1219)
- Chen, H.-W., Prochaska, J. X., Weiner, B. J., Mulchaey, J. S., & Williger, G. M. 2005, *ApJL*, 629, L25, doi: [10.1086/444377](https://doi.org/10.1086/444377)
- Chiang, Y.-K., Overzier, R. A., Gebhardt, K., et al. 2015, *ApJ*, 808, 37, doi: [10.1088/0004-637X/808/1/37](https://doi.org/10.1088/0004-637X/808/1/37)
- Cowley, M. J., Spitler, L. R., Tran, K.-V. H., et al. 2016, *MNRAS*, 457, 629, doi: [10.1093/mnras/stv2992](https://doi.org/10.1093/mnras/stv2992)
- Crighton, N. H. M., Bielby, R., Shanks, T., et al. 2011, *MNRAS*, 414, 28, doi: [10.1111/j.1365-2966.2011.17247.x](https://doi.org/10.1111/j.1365-2966.2011.17247.x)
- Croft, R. A. C., Miralda-Escudé, J., Zheng, Z., Blomqvist, M., & Pieri, M. 2018, *MNRAS*, 481, 1320, doi: [10.1093/mnras/sty2302](https://doi.org/10.1093/mnras/sty2302)
- Croft, R. A. C., Miralda-Escudé, J., Zheng, Z., et al. 2016, *MNRAS*, 457, 3541, doi: [10.1093/mnras/stw204](https://doi.org/10.1093/mnras/stw204)
- Cucciati, O., Zamorani, G., Lemaux, B. C., et al. 2014, *A&A*, 570, A16, doi: [10.1051/0004-6361/201423811](https://doi.org/10.1051/0004-6361/201423811)
- Dawson, K. S., Schlegel, D. J., Ahn, C. P., et al. 2013, *AJ*, 145, 10, doi: [10.1088/0004-6256/145/1/10](https://doi.org/10.1088/0004-6256/145/1/10)
- Dekel, A., Zolotov, A., Tweed, D., et al. 2013, *MNRAS*, 435, 999, doi: [10.1093/mnras/stt1338](https://doi.org/10.1093/mnras/stt1338)
- Dickinson, M., Stern, D., Giavalisco, M., et al. 2004, *ApJL*, 600, L99, doi: [10.1086/381119](https://doi.org/10.1086/381119)
- Diener, C., Lilly, S. J., Ledoux, C., et al. 2015, *ApJ*, 802, 31, doi: [10.1088/0004-637X/802/1/31](https://doi.org/10.1088/0004-637X/802/1/31)
- Dijkstra, M., Lidz, A., & Wyithe, J. S. B. 2007, *MNRAS*, 377, 1175, doi: [10.1111/j.1365-2966.2007.11666.x](https://doi.org/10.1111/j.1365-2966.2007.11666.x)
- D'Odorico, V., Bruscoli, M., Saitta, F., et al. 2008, *MNRAS*, 389, 1727, doi: [10.1111/j.1365-2966.2008.13611.x](https://doi.org/10.1111/j.1365-2966.2008.13611.x)
- Eisenstein, D. J., Weinberg, D. H., Agol, E., et al. 2011, *AJ*, 142, 72, doi: [10.1088/0004-6256/142/3/72](https://doi.org/10.1088/0004-6256/142/3/72)
- Erb, D. K., Steidel, C. C., Trainor, R. F., et al. 2014, *ApJ*, 795, 33, doi: [10.1088/0004-637X/795/1/33](https://doi.org/10.1088/0004-637X/795/1/33)
- Faucher-Giguère, C.-A., Prochaska, J. X., Lidz, A., Hernquist, L., & Zaldarriaga, M. 2008, *ApJ*, 681, 831, doi: [10.1086/588648](https://doi.org/10.1086/588648)
- Finkelstein, S. L., Hill, G. J., Gebhardt, K., et al. 2011, *ApJ*, 729, 140, doi: [10.1088/0004-637X/729/2/140](https://doi.org/10.1088/0004-637X/729/2/140)
- Font-Ribera, A., Miralda-Escudé, J., Arnau, E., et al. 2012, *JCAP*, 2012, 059, doi: [10.1088/1475-7516/2012/11/059](https://doi.org/10.1088/1475-7516/2012/11/059)
- Font-Ribera, A., Arnau, E., Miralda-Escudé, J., et al. 2013, *JCAP*, 2013, 018, doi: [10.1088/1475-7516/2013/05/018](https://doi.org/10.1088/1475-7516/2013/05/018)
- Furusawa, H., Kosugi, G., Akiyama, M., et al. 2008, *ApJS*, 176, 1, doi: [10.1086/527321](https://doi.org/10.1086/527321)
- Guaita, L., Gawiser, E., Padilla, N., et al. 2010, *ApJ*, 714, 255, doi: [10.1088/0004-637X/714/1/255](https://doi.org/10.1088/0004-637X/714/1/255)
- Guaita, L., Acquaviva, V., Padilla, N., et al. 2011, *ApJ*, 733, 114, doi: [10.1088/0004-637X/733/2/114](https://doi.org/10.1088/0004-637X/733/2/114)
- Gunn, J. E., & Peterson, B. A. 1965, *ApJ*, 142, 1633, doi: [10.1086/148444](https://doi.org/10.1086/148444)
- Hagen, A., Ciardullo, R., Gronwall, C., et al. 2014, *ApJ*, 786, 59, doi: [10.1088/0004-637X/786/1/59](https://doi.org/10.1088/0004-637X/786/1/59)
- Hagen, A., Zeimann, G. R., Behrens, C., et al. 2016, *ApJ*, 817, 79, doi: [10.3847/0004-637X/817/1/79](https://doi.org/10.3847/0004-637X/817/1/79)
- Haiman, Z. 2002, *ApJL*, 576, L1, doi: [10.1086/343101](https://doi.org/10.1086/343101)
- Hashimoto, T., Ouchi, M., Shimasaku, K., et al. 2013, *ApJ*, 765, 70, doi: [10.1088/0004-637X/765/1/70](https://doi.org/10.1088/0004-637X/765/1/70)
- Hashimoto, T., Verhamme, A., Ouchi, M., et al. 2015, *ApJ*, 812, 157, doi: [10.1088/0004-637X/812/2/157](https://doi.org/10.1088/0004-637X/812/2/157)
- Hasinger, G., Capak, P., Salvato, M., et al. 2018, *ApJ*, 858, 77, doi: [10.3847/1538-4357/aabacf](https://doi.org/10.3847/1538-4357/aabacf)
- Hatziminaoglou, E., Omont, A., Stevens, J. A., et al. 2010, *A&A*, 518, L33, doi: [10.1051/0004-6361/201014679](https://doi.org/10.1051/0004-6361/201014679)
- Hayashino, T., Inoue, A. K., Kousai, K., et al. 2019, *MNRAS*, 484, 5868, doi: [10.1093/mnras/stz388](https://doi.org/10.1093/mnras/stz388)
- Hickox, R. C., Wardlow, J. L., Smail, I., et al. 2012, *MNRAS*, 421, 284, doi: [10.1111/j.1365-2966.2011.20303.x](https://doi.org/10.1111/j.1365-2966.2011.20303.x)
- Hopkins, P. F., Hernquist, L., Cox, T. J., & Kereš, D. 2008, *ApJS*, 175, 356, doi: [10.1086/524362](https://doi.org/10.1086/524362)
- Ichikawa, K., Ueda, Y., Terashima, Y., et al. 2012, *ApJ*, 754, 45, doi: [10.1088/0004-637X/754/1/45](https://doi.org/10.1088/0004-637X/754/1/45)
- Ilbert, O., Arnouts, S., McCracken, H. J., et al. 2006, *A&A*, 457, 841, doi: [10.1051/0004-6361:20065138](https://doi.org/10.1051/0004-6361:20065138)
- Kakuma, R., Ouchi, M., Harikane, Y., et al. 2019, arXiv e-prints. <https://arxiv.org/abs/1906.00173>
- Khostovan, A. A., Sobral, D., Mobasher, B., et al. 2018, *MNRAS*, 478, 2999, doi: [10.1093/mnras/sty925](https://doi.org/10.1093/mnras/sty925)
- . 2019, *MNRAS*, 489, 555, doi: [10.1093/mnras/stz2149](https://doi.org/10.1093/mnras/stz2149)
- Konno, A., Ouchi, M., Nakajima, K., et al. 2016, *ApJ*, 823, 20, doi: [10.3847/0004-637X/823/1/20](https://doi.org/10.3847/0004-637X/823/1/20)
- Koutoulidis, L., Plionis, M., Georgantopoulos, I., & Fanidakis, N. 2013, *MNRAS*, 428, 1382, doi: [10.1093/mnras/sts119](https://doi.org/10.1093/mnras/sts119)

- Kriek, M., Shapley, A. E., Reddy, N. A., et al. 2015, *ApJS*, 218, 15, doi: [10.1088/0067-0049/218/2/15](https://doi.org/10.1088/0067-0049/218/2/15)
- Kusakabe, H., Shimasaku, K., Nakajima, K., & Ouchi, M. 2015, *ApJL*, 800, L29, doi: [10.1088/2041-8205/800/2/L29](https://doi.org/10.1088/2041-8205/800/2/L29)
- Kusakabe, H., Shimasaku, K., Ouchi, M., et al. 2018, *PASJ*, 70, 4, doi: [10.1093/pasj/psx148](https://doi.org/10.1093/pasj/psx148)
- Kusakabe, H., Shimasaku, K., Momose, R., et al. 2019, *PASJ*, 71, 55, doi: [10.1093/pasj/psz029](https://doi.org/10.1093/pasj/psz029)
- Laigle, C., McCracken, H. J., Ilbert, O., et al. 2016, *ApJS*, 224, 24, doi: [10.3847/0067-0049/224/2/24](https://doi.org/10.3847/0067-0049/224/2/24)
- Le Fèvre, O., Tasca, L. A. M., Cassata, P., et al. 2015, *A&A*, 576, A79, doi: [10.1051/0004-6361/201423829](https://doi.org/10.1051/0004-6361/201423829)
- Lee, K.-G., Hennawi, J. F., Stark, C., et al. 2014, *ApJL*, 795, L12, doi: [10.1088/2041-8205/795/1/L12](https://doi.org/10.1088/2041-8205/795/1/L12)
- Lee, K.-G., Hennawi, J. F., White, M., et al. 2016, *ApJ*, 817, 160, doi: [10.3847/0004-637X/817/2/160](https://doi.org/10.3847/0004-637X/817/2/160)
- Lee, K.-G., Krolewski, A., White, M., et al. 2018, *ApJS*, 237, 31, doi: [10.3847/1538-4365/aace58](https://doi.org/10.3847/1538-4365/aace58)
- Lilly, S. J., Le Fèvre, O., Renzini, A., et al. 2007, *ApJS*, 172, 70, doi: [10.1086/516589](https://doi.org/10.1086/516589)
- Lilly, S. J., Le Brun, V., Maier, C., et al. 2009, *ApJS*, 184, 218, doi: [10.1088/0067-0049/184/2/218](https://doi.org/10.1088/0067-0049/184/2/218)
- Lusso, E., Comastri, A., Simmons, B. D., et al. 2012, *MNRAS*, 425, 623, doi: [10.1111/j.1365-2966.2012.21513.x](https://doi.org/10.1111/j.1365-2966.2012.21513.x)
- Masters, D. C., Stern, D. K., Cohen, J. G., et al. 2017, *ApJ*, 841, 111, doi: [10.3847/1538-4357/aa6f08](https://doi.org/10.3847/1538-4357/aa6f08)
- Mawatari, K., Inoue, A. K., Yamada, T., et al. 2017, *MNRAS*, 467, 3951, doi: [10.1093/mnras/stx038](https://doi.org/10.1093/mnras/stx038)
- McLinden, E. M., Finkelstein, S. L., Rhoads, J. E., et al. 2011, *ApJ*, 730, 136, doi: [10.1088/0004-637X/730/2/136](https://doi.org/10.1088/0004-637X/730/2/136)
- Meyer, R. A., Bosman, S. E. I., Kakiichi, K., & Ellis, R. S. 2019a, *MNRAS*, 483, 19, doi: [10.1093/mnras/sty2954](https://doi.org/10.1093/mnras/sty2954)
- Meyer, R. A., Kakiichi, K., Bosman, S. E. I., et al. 2019b, arXiv e-prints, arXiv:1912.04314.  
<https://arxiv.org/abs/1912.04314>
- Michałowski, M. J., Dunlop, J. S., Koprowski, M. P., et al. 2017, *MNRAS*, 469, 492, doi: [10.1093/mnras/stx861](https://doi.org/10.1093/mnras/stx861)
- Miralda-Escudé, J., Cen, R., Ostriker, J. P., & Rauch, M. 1996, *ApJ*, 471, 582, doi: [10.1086/177992](https://doi.org/10.1086/177992)
- Momcheva, I. G., Brammer, G. B., van Dokkum, P. G., et al. 2016, *ApJS*, 225, 27, doi: [10.3847/0067-0049/225/2/27](https://doi.org/10.3847/0067-0049/225/2/27)
- Momose, R., Shimizu, I., Nagamine, K., et al. 2020, arXiv e-prints, arXiv:2002.07334.  
<https://arxiv.org/abs/2002.07334>
- Mukae, S., Ouchi, M., Kakiichi, K., et al. 2017, *ApJ*, 835, 281, doi: [10.3847/1538-4357/835/2/281](https://doi.org/10.3847/1538-4357/835/2/281)
- Mukae, S., Ouchi, M., Cai, Z., et al. 2020, *ApJ*, 896, 45, doi: [10.3847/1538-4357/ab8db7](https://doi.org/10.3847/1538-4357/ab8db7)
- Muzzin, A., Marchesini, D., Stefanon, M., et al. 2013, *ApJS*, 206, 8, doi: [10.1088/0067-0049/206/1/8](https://doi.org/10.1088/0067-0049/206/1/8)
- Myers, A. D., Brunner, R. J., Nichol, R. C., et al. 2007, *ApJ*, 658, 85, doi: [10.1086/511519](https://doi.org/10.1086/511519)
- Nakajima, K., Ouchi, M., Shimasaku, K., et al. 2013, *ApJ*, 769, 3, doi: [10.1088/0004-637X/769/1/3](https://doi.org/10.1088/0004-637X/769/1/3)
- . 2012, *ApJ*, 745, 12, doi: [10.1088/0004-637X/745/1/12](https://doi.org/10.1088/0004-637X/745/1/12)
- Nanayakkara, T., Glazebrook, K., Kacprzak, G. G., et al. 2016, *ApJ*, 828, 21, doi: [10.3847/0004-637X/828/1/21](https://doi.org/10.3847/0004-637X/828/1/21)
- Oke, J. B., Cohen, J. G., Carr, M., et al. 1995, *PASP*, 107, 375, doi: [10.1086/133562](https://doi.org/10.1086/133562)
- Pérez-Ràfols, I., Font-Ribera, A., Miralda-Escudé, J., et al. 2018, *MNRAS*, 473, 3019, doi: [10.1093/mnras/stx2525](https://doi.org/10.1093/mnras/stx2525)
- Plionis, M., Koutoulidis, L., Koulouridis, E., et al. 2018, *A&A*, 620, A17, doi: [10.1051/0004-6361/201832970](https://doi.org/10.1051/0004-6361/201832970)
- Prochaska, J. X., Hennawi, J. F., Lee, K.-G., et al. 2013, *ApJ*, 776, 136, doi: [10.1088/0004-637X/776/2/136](https://doi.org/10.1088/0004-637X/776/2/136)
- Rakic, O., Schaye, J., Steidel, C. C., & Rudie, G. C. 2011, *MNRAS*, 414, 3265, doi: [10.1111/j.1365-2966.2011.18624.x](https://doi.org/10.1111/j.1365-2966.2011.18624.x)
- . 2012, *ApJ*, 751, 94, doi: [10.1088/0004-637X/751/2/94](https://doi.org/10.1088/0004-637X/751/2/94)
- Rauch, M. 1998, *ARA&A*, 36, 267, doi: [10.1146/annurev.astro.36.1.267](https://doi.org/10.1146/annurev.astro.36.1.267)
- Rubin, K. H. R., Hennawi, J. F., Prochaska, J. X., et al. 2015, *ApJ*, 808, 38, doi: [10.1088/0004-637X/808/1/38](https://doi.org/10.1088/0004-637X/808/1/38)
- Rudie, G. C., Steidel, C. C., Trainor, R. F., et al. 2012, *ApJ*, 750, 67, doi: [10.1088/0004-637X/750/1/67](https://doi.org/10.1088/0004-637X/750/1/67)
- Ryan-Weber, E. V. 2006, *MNRAS*, 367, 1251, doi: [10.1111/j.1365-2966.2006.10010.x](https://doi.org/10.1111/j.1365-2966.2006.10010.x)
- Santos, M. R. 2004, *MNRAS*, 349, 1137, doi: [10.1111/j.1365-2966.2004.07594.x](https://doi.org/10.1111/j.1365-2966.2004.07594.x)
- Scoville, N., Aussel, H., Brusa, M., et al. 2007, *The Astrophysical Journal Supplement Series*, 172, 1, doi: [10.1086/516585](https://doi.org/10.1086/516585)
- Shi, K., Huang, Y., Lee, K.-S., et al. 2019, *ApJ*, 879, 9, doi: [10.3847/1538-4357/ab2118](https://doi.org/10.3847/1538-4357/ab2118)
- Shibuya, T., Ouchi, M., Nakajima, K., et al. 2014, *ApJ*, 788, 74, doi: [10.1088/0004-637X/788/1/74](https://doi.org/10.1088/0004-637X/788/1/74)
- Shimakawa, R., Kodama, T., Shibuya, T., et al. 2017a, *MNRAS*, 468, 1123, doi: [10.1093/mnras/stx091](https://doi.org/10.1093/mnras/stx091)
- Shimakawa, R., Kodama, T., Hayashi, M., et al. 2017b, *MNRAS*, 468, L21, doi: [10.1093/mnrasl/slx019](https://doi.org/10.1093/mnrasl/slx019)
- Smolčić, V., Aravena, M., Navarrete, F., et al. 2012, *A&A*, 548, A4, doi: [10.1051/0004-6361/201219368](https://doi.org/10.1051/0004-6361/201219368)
- Sobral, D., Smail, I., Best, P. N., et al. 2013a, *MNRAS*, 428, 1128, doi: [10.1093/mnras/sts096](https://doi.org/10.1093/mnras/sts096)
- . 2013b, *MNRAS*, 428, 1128, doi: [10.1093/mnras/sts096](https://doi.org/10.1093/mnras/sts096)
- Sobral, D., Matthee, J., Darvish, B., et al. 2018, *MNRAS*, 477, 2817, doi: [10.1093/mnras/sty782](https://doi.org/10.1093/mnras/sty782)

- Song, M., Finkelstein, S. L., Gebhardt, K., et al. 2014, *ApJ*, 791, 3, doi: [10.1088/0004-637X/791/1/3](https://doi.org/10.1088/0004-637X/791/1/3)
- Stark, C. W., White, M., Lee, K.-G., & Hennawi, J. F. 2015, *MNRAS*, 453, 311, doi: [10.1093/mnras/stv1620](https://doi.org/10.1093/mnras/stv1620)
- Steidel, C. C., Shapley, A. E., Pettini, M., et al. 2004, *ApJ*, 604, 534, doi: [10.1086/381960](https://doi.org/10.1086/381960)
- Straatman, C. M. S., Spitler, L. R., Quadri, R. F., et al. 2016, *ApJ*, 830, 51, doi: [10.3847/0004-637X/830/1/51](https://doi.org/10.3847/0004-637X/830/1/51)
- Suh, H., Civano, F., Hasinger, G., et al. 2019, *ApJ*, 872, 168, doi: [10.3847/1538-4357/ab01fb](https://doi.org/10.3847/1538-4357/ab01fb)
- Tejos, N., Morris, S. L., Finn, C. W., et al. 2014, *MNRAS*, 437, 2017, doi: [10.1093/mnras/stt1844](https://doi.org/10.1093/mnras/stt1844)
- Toshikawa, J., Kashikawa, N., Overzier, R., et al. 2016, *ApJ*, 826, 114, doi: [10.3847/0004-637X/826/2/114](https://doi.org/10.3847/0004-637X/826/2/114)
- Trump, J. R., Impey, C. D., Elvis, M., et al. 2009, *ApJ*, 696, 1195, doi: [10.1088/0004-637X/696/2/1195](https://doi.org/10.1088/0004-637X/696/2/1195)
- Tummuangpak, P., Bielby, R. M., Shanks, T., et al. 2014, *MNRAS*, 442, 2094, doi: [10.1093/mnras/stu828](https://doi.org/10.1093/mnras/stu828)
- Turner, M. L., Schaye, J., Steidel, C. C., Rudie, G. C., & Strom, A. L. 2014, *MNRAS*, 445, 794, doi: [10.1093/mnras/stu1801](https://doi.org/10.1093/mnras/stu1801)
- Uchiyama, H., Kashikawa, N., Overzier, R., et al. 2019, *ApJ*, 870, 45, doi: [10.3847/1538-4357/aaf7b](https://doi.org/10.3847/1538-4357/aaf7b)
- Umehata, H., Fumagalli, M., Smail, I., et al. 2019, *Science*, 366, 97, doi: [10.1126/science.aaw5949](https://doi.org/10.1126/science.aaw5949)
- van der Wel, A., Noeske, K., Bezanson, R., et al. 2016, *ApJS*, 223, 29, doi: [10.3847/0067-0049/223/2/29](https://doi.org/10.3847/0067-0049/223/2/29)
- Wei, A., Kovács, A., Coppin, K., et al. 2009, *ApJ*, 707, 1201, doi: [10.1088/0004-637X/707/2/1201](https://doi.org/10.1088/0004-637X/707/2/1201)
- Wilman, R. J., Morris, S. L., Jannuzi, B. T., Davé, R., & Shone, A. M. 2007, *MNRAS*, 375, 735, doi: [10.1111/j.1365-2966.2006.11342.x](https://doi.org/10.1111/j.1365-2966.2006.11342.x)